J. Fluid Mech. (2006), *vol.* 553, *pp.* 347–388.
doi:10.1017/S0022112006009025 Printed in the United Kingdom

The growth of concentration fluctuations in dilute dispersions of orientable and deformable particles under sedimentation

By DAVID SAINTILLAN[1], ERIC S. G. SHAQFEH[1,2,3] AND ERIC DARVE[1,3]

[1]Department of Mechanical Engineering, Stanford University, Stanford, CA 94305, USA
[2]Department of Chemical Engineering, Stanford University, Stanford, CA 94305, USA
[3]Institute for Computational and Mathematical Engineering, Stanford University, Stanford, CA 94305, USA

(Received 11 April 2005 and in revised form 12 October 2005)

Theory and numerical simulations are used to investigate the concentration fluctuations and the microstructure in dilute sedimenting suspensions of orientable and deformable particles at zero Reynolds number. The case of orientable particles is studied using prolate and oblate spheroids, while viscous droplets in the small deformation regime illustrate the effects of deformability. An efficient method based on a point-particle approximation and on smooth localized force representations is implemented to simulate full-scale suspensions with both periodic and slip boundaries, where the latter are used to qualitatively reproduce the effects of horizontal walls. The concentration instability predicted theoretically for suspensions of spheroids is captured in the simulations, and we find that including horizontal walls provides a mechanism for wavenumber selection, in contrast to periodic systems in which the longest wavelength set by the size of the container dominates. A theoretical model for the case of slightly deformable particles is developed, and a linear stability analysis shows that such suspensions are also unstable to concentration fluctuations under sedimentation. In the absence of diffusion, the model predicts that density fluctuations are equally unstable at all wavelengths, but we show that diffusion, whether Brownian or hydrodynamic, should damp high-wavenumber fluctuations. Simulations are also performed for deformable particles, and again an instability is observed that shows a similar mechanism for the wavenumber selection in finite containers. Our results demonstrate that all sedimentation processes of orientable or deformable particles are subject to spontaneous concentration inhomogeneities, which control the sedimentation rates in these systems.

1. Introduction

Although conceptually simple, the steady sedimentation of a dilute dispersion of particles in a liquid at low Reynolds number remains an unresolved problem of non-equilibrium statistical mechanics (Ramaswamy 2001). Even in the simplest case of a random dilute dispersion of spheres, a simple physical argument suggests that the velocity variance should diverge, growing unbounded with the linear dimension of the sedimenting system: $\langle \Delta v^2 \rangle \sim L$ (Caflisch & Luke 1985; Hinch 1987). Since the work of Caflisch & Luke numerous experiments have tried to test this scaling, but typically manifest a saturation of the velocity fluctuations in contrast with the

theoretical prediction (Nicolai and Guazzelli 1995; Segrè, Herbolzheimer & Chaikin 1997; Bergougnoux *et al.* 2003). Precise particle image velocimetry measurements by Guazzelli (2001) in fact showed the following: during the early period after the cessation of mixing, large recirculation vortices of the size of the container are observed, confirming the Caflisch & Luke argument, but these quickly decay and give way to smaller less intense vortices and velocity fluctuations that are independent of the container dimensions.

Several theoretical explanations have been proposed to resolve this contradiction, most of which relax one of the fundamental assumptions of the original argument, namely homogeneity. The close relationship between the microstructural arrangement of the particles in the suspension and the velocity fluctuations was first highlighted by Koch & Shaqfeh (1991), who related the amplitude of the velocity fluctuations to the structure factor of the suspension, which is the Fourier transform of the pair probability function. Koch & Shaqfeh then argued that a specific form of the pair probability function, in which there is a net deficit of neighbouring particles in the vicinity of each particle, would lead to a screening of the velocity disturbance as a result of three-particle hydrodynamic interactions, and is therefore a potential mechanism for the saturation of the velocity fluctuations. This mechanism, however, has not been verified, and is not consistent with more recent results from numerical simulations, which do show a decay of the velocity fluctuations (e.g. Ladd 2002; Nguyen & Ladd 2004, 2005; Mucha *et al.* 2004).

The key idea that microstructural changes occurring during sedimentation are responsible for the decay of the velocity fluctuations is supported by experiments by Lei, Ackerson & Tong (2001), which showed the suppression of random number density fluctuations during sedimentation. Two mechanisms have been suggested for this suppression. Following an original idea by Luke (2000), it has been argued that a small vertical stratification in the suspension may be responsible for the decay (Mucha & Brenner 2003; Mucha *et al.* 2004). More precisely, Mucha *et al.* suggest that in thin cells in which stratification is weak, the velocity fluctuations scale with the thin dimension, whereas in larger cells, stratification is more significant and causes the decay of the fluctuations. Experiments by the same authors seemed to confirm this mechanism (Tee *et al.* 2002; Mucha *et al.* 2004), although such a strong stratification was not observed in other studies (Bergougnoux *et al.* 2003), suggesting that polydispersity in the size of the particles may have been a factor. Recent lattice-Boltzmann simulations by Nguyen & Ladd (2004, 2005) also captured the suppression of the number density fluctuations, but did not show any significant broadening of the front.

A second explanation was proposed by Hinch (1987): in a finite cell with a bottom wall, random density fluctuations create strong convection currents spanning the width of the cell, which should lead to a homogenization and may remove the horizontal fluctuations in the number density. If this process continues down to the interparticle separation length scale, the final velocity fluctuations may no longer depend on the system dimensions. The mechanism speculated by Hinch is supported by the observations of Guazzelli (2001) described previously, in which large recirculation cells in the initial instants of the experiments are observed to decay. The importance of the role of the bottom wall was also emphasized by Ladd using lattice-Boltzmann simulations: in periodic systems, Ladd observes the divergence of the velocity fluctuations without any microstructural changes (Ladd 1996), whereas in systems bounded by horizontal walls the velocity variance is found to saturate and the horizontal density fluctuations are strongly suppressed (Ladd 2002; Nguyen & Ladd 2004, 2005).

The cases of non-spherical or non-rigid particles, which we address in this paper, have received much less attention in the past, in spite of their common occurrence both in natural phenomena and industrial applications. One illustrative example in which both anisotropy and deformability play a significant role is the sedimentation of red blood cells, which is a widely used tool for the screening of diseases (Reinhart, Singh & Werner 1989). Other examples are as diverse as the separation of biological macromolecules by centrifugation, the fabrication of fibre-reinforced materials, or the treatment of waste materials.

It is unclear *a priori* how anisotropy or deformability will influence the physical mechanism described above, by which the suppression of number density fluctuations leads to a decay of the velocity variance in suspensions of spheres. The fundamental difference between anisotropic and isotropic particles is that the former orient in flow, and, depending on their orientation, can migrate in the directions perpendicular to gravity. Koch & Shaqfeh (1989) first studied this coupling between the velocity fluctuations and the anisotropic mobility of the particles for dispersions of spheroids. They modelled the suspension with continuum variables, and using a linear stability analysis they showed that small density fluctuations at low wavenumbers should amplify. They proposed a simple physical mechanism: the disturbance flow induced by the density fluctuations causes the particles to orient in such a way that they migrate towards the regions of higher particle density. Based on a linearized model for an unbounded fluid, the theory of Koch & Shaqfeh (1989) predicted that the longest wavelengths should grow the fastest.

The sedimentation of fibre suspensions, which behave like high-aspect-ratio spheroids, has been the subject of a few experimental studies, some of which confirmed the instability predicted by Koch & Shaqfeh (1989). Kumar & Ramarao (1991) reported the formation of large floc-like structures in dilute suspensions, settling at larger velocities; at higher concentrations, interaction between the flocs was observed to cause velocity hindrance. Later, Turney *et al.* (1995) used magnetic resonance imaging to determine the mean sedimentation velocity in concentrated suspensions of rodlike particles; they reported velocity hindrance, but did not provide any information on the homogeneity of the bulk.

Herzhaft *et al.* (1996) and Herzhaft & Guazzelli (1999) studied the sedimentation of fibres in the dilute and semi-dilute regimes, in which the instability can be expected to be the strongest. They adapted a particle-tracking technique previously used for sphere suspensions (Ham & Homsy 1988; Nicolai *et al.* 1995), in which the position, orientation and velocity of a few silver-coated particles are measured, while the remainder of the particles are made invisible by matching their index of refraction with the index of the solvent. They observed that the particles strongly oriented in the direction of gravity, with occasional flipping between the two vertical orientations. They also reported an increase in the mean velocity in the dilute regime beyond the maximum velocity of an isolated vertical fibre, followed by velocity hindrance in the semi-dilute regime. The velocity fluctuations measured were typically very large, up to one order of magnitude larger than the mean velocity in the semi-dilute regime. While no systematic investigation of the microstructure was undertaken, snapshots of the suspension suggested that the particles gathered to form dense clusters or streamers slightly elongated in the direction of gravity and surrounded by clarified fluid; the size of the clusters, although not measured precisely, was estimated to be of the order of a few particle lengths.

The sedimentation of axisymmetric particles was also tackled in a few computational studies, with varying degrees of approximation. Mackaplow &

Shaqfeh (1998) performed dynamic simulations of fibre sedimentation at zero Reynolds number with periodic boundary conditions, in which they approximated the disturbance of a given particle on the fluid by a point force. Although very simple, their model captured all the salient features of the instability: the fibres were observed to converge towards one dense streamer and to orient vertically. The orientation distributions were found to reach a steady state, the mean velocity, however, kept increasing and did not show any signs of saturation. Butler & Shaqfeh (2002) devised a more sophisticated method in which the fibres were represented by line distributions of point forces, which were linearized to capture correctly the total force, total torque and stresslet on each particle; they also included close particle hydrodynamic interactions through lubrication forces, and excluded volume interactions using short-range repulsive forces. Their simulations greatly improved on the results of Mackaplow & Shaqfeh (1998), and reasonable agreement with the experimental data of Herzhaft & Guazzelli (1999) was found using very elongated boxes in the direction of gravity. In particular, such boxes allowed the mean velocity to reach a steady state. The effects of inertia were also considered by Kuusela and coworkers, who performed simulations of the sedimentation of spheroids at small but finite Reynolds number (Kuusela, Höfler & Schwarzer 2001; Kuusela, Lahtinen & Ala-Nissila 2003). The principal effect of inertia was on the orientation distributions, which showed a preferential alignment in the horizontal direction in very dilute dispersions, followed by a transition towards a vertical alignment at higher concentrations. The mean velocities showed qualitative agreement with the inertialess experiments of Herzhaft & Guazzelli (1999); clustering was reported, although no further information was given on the structure of the suspension.

In an attempt to study more precisely the microstructure in suspensions of sedimenting fibres, we recently improved the simulation method of Butler & Shaqfeh (2002) by implementing a smooth particle-mesh Ewald algorithm, allowing the efficient computation of the far-field hydrodynamic interactions (Saintillan, Darve & Shaqfeh 2005). This fast algorithm allowed us to simulate up to 512 particles, providing new insight into the large-scale collective dynamics and their coupling to the disturbance flow. In particular, in our periodic systems we found that the formation of dense clusters was directly linked to the initial disturbance flow in the fluid, which is typically dominated by low-wavenumber fluctuations, therefore resulting in the formation of a unique streamer in most simulations. We speculated that the presence of a bottom wall may play a role in selecting a wavelength for the instability, by breaking the initial low-wavenumber fluctuations in the same way as is observed in sphere suspensions (Guazzelli 2001; Ladd 2002). This mechanism remained an open question: while the presence of a bottom wall may indeed lead to a homogenization, and result in a decay of the large-scale fluctuations, the instability, on the contrary, feeds the inhomogeneities; the balance between these two effects is difficult to predict and is addressed in this paper. Our recent work also showed the difficulty in reaching a steady-state simulation in large periodic systems: even after the instability had picked a wavelength, streamers were observed to become denser and denser, resulting in the steady increase of the mean velocity. The assumption that a steady state indeed exists, which is the basis for simulations with periodic boundary conditions, therefore deserves closer attention.

Deformable particles such as drops or bubbles share qualitative similarities with orientable particles, and there has been recent evidence suggesting that an instability similar to that predicted by Koch & Shaqfeh (1989) for spheroids may also occur in such systems. This was first suggested by Manga & Stone (1995), who pointed

out that the deformation of rising bubbles as a result of hydrodynamic interactions should result in a migration towards the regions of high density. They illustrated this mechanism using a similar picture to that in Koch & Shaqfeh (1989), but made no further attempt to study the instability. In spite of the clear analogy between the two situations, the instability for drops, if it exists, is slightly more complex as the deformations leading to the lateral migration are themselves induced by the density fluctuations through the disturbance field. To our knowledge, the instability for drops has never been reported in an experiment, but a few computational studies seem to confirm its existence. Zinchenko & Davis (2000, 2003) performed boundary integral simulations of concentrated suspensions of deformable drops under sedimentation. Starting from random configurations of spherical drops, they observed that the drops acquired prolate shapes and oriented in the direction of gravity, resulting in an increase of the sedimentation rate. Again clustering was observed, but no detailed study of the suspension structure was performed.

In this work we study the microstructure and concentration fluctuations in sedimenting suspensions of orientable and deformable particles, focusing on the coupling between the large-scale fluctuations in the concentration and velocity fields and on the influence of solid boundaries. In particular, we wish to determine whether a steady-state structure can be achieved in such suspensions and identify the mechanisms affecting this structure. We investigate two different types of particle: rigid spheroids are used as prototypes of orientable particles, whereas viscous drops within the small deformation theory (Cox 1969; Haber & Hetsroni 1971) are used to illustrate the case of deformable particles. The paper is organized as follows. In § 2, we treat the case of orientable particles: an efficient method is described to simulate realistic-size systems of sedimenting spheroids, both in periodic and non-periodic domains. Results are presented on the suspension microstructure and on velocity and orientation statistics. The case of deformable particles is addressed in § 3: we first develop a model for such suspensions and perform a linear stability analysis to show that concentration fluctuations are indeed unstable; the simulation method described in § 2 is then adapted to the case of slightly deformed drops and is used to investigate the pattern formation. The results are summarized in § 4.

2. Orientable particles

2.1. *Method of simulation*

Motivated by the conclusions of our previous work on suspensions of rigid fibres (Saintillan *et al.* 2005), we have developed an efficient method allowing the simulation of suspensions of realistic sizes in both periodic and bounded geometries. The method is based on a point-force approximation which is analogous to the original model of Koch & Shaqfeh (1989) and to the point-fibre simulations of Mackaplow & Shaqfeh (1998). However, the disturbance velocity is calculated numerically from the Stokes equations using smooth localized force representations in a similar manner as in the force-coupling method of Lomholt & Maxey (2003); this approximate method allows for a very efficient calculation of the velocities in various boundary conditions while removing the singularities from the disturbance field.

2.1.1. *Dynamic equations*

We consider a system of N spheroids of aspect ratio A in a box of dimensions $L_x \times L_y \times L_z$, where gravity points in the vertical direction: $\boldsymbol{g} = -g\hat{\boldsymbol{z}}$. The configuration of a given particle $\alpha = 1, \ldots, N$ is entirely determined by the

position $\boldsymbol{x}_\alpha$ of its centre of mass and by a unit vector $\boldsymbol{p}_\alpha$ aligned with its major axis. In the dilute limit, the disturbance velocity induced by the motion of the particles varies over length scales that are much larger than the size of a particle, so that locally the flow field experienced by a given spheroid can be approximated as:

$$\boldsymbol{u}(\boldsymbol{x}) \approx \boldsymbol{u}(\boldsymbol{x}_\alpha) + \nabla\boldsymbol{u}(\boldsymbol{x}_\alpha)\cdot(\boldsymbol{x}-\boldsymbol{x}_\alpha) + \cdots \quad \text{for} \quad |\boldsymbol{x}-\boldsymbol{x}_\alpha| \ll L, \tag{2.1}$$

where L is the characteristic length for the variation of the velocity. Typically, this characteristic length is the mean interparticle distance $L = n^{-1/3}$, where n is the number density in the suspension. Under this approximation, the translational velocity of a particle is calculated as the sum of its settling velocity $\boldsymbol{U}_s$ in orientation $\boldsymbol{p}_\alpha$ and of the disturbance velocity $\boldsymbol{u}$ evaluated at its centre of mass:

$$\dot{\boldsymbol{x}}_\alpha = \boldsymbol{U}_s(\boldsymbol{p}_\alpha) + \boldsymbol{u}(\boldsymbol{x}_\alpha). \tag{2.2}$$

The settling velocity in a pure fluid is the product of the particle mobility by the gravity force acting upon the particle, and for a spheroid is written as

$$\boldsymbol{U}_s(\boldsymbol{p}_\alpha) = \frac{1}{8\pi\mu l}(\beta_0\boldsymbol{I} + \beta_1\boldsymbol{p}_\alpha\boldsymbol{p}_\alpha)\cdot\boldsymbol{F}. \tag{2.3}$$

μ is the viscosity of the solvent, l is the length of the major axis of a particle, and the gravity force is $\boldsymbol{F} = \Delta\rho V_p\boldsymbol{g}$ where $\Delta\rho$ is the relative density and $V_p = \pi l^3/6A^2$ is the volume of a particle. β_0 and β_1 are dimensionless functions of the aspect ratio defined for arbitrary A and can be found elsewhere (see for instance Happel & Brenner 1965, or Koch & Shaqfeh 1989). The rotational motion of the particle is described using Jeffery's equation (Jeffery 1922):

$$\dot{\boldsymbol{p}}_\alpha = (\boldsymbol{I}-\boldsymbol{p}_\alpha\boldsymbol{p}_\alpha)\cdot\left(\frac{A^2-1}{A^2+1}\boldsymbol{E}(\boldsymbol{x}_\alpha) + \boldsymbol{\Omega}(\boldsymbol{x}_\alpha)\right)\cdot\boldsymbol{p}_\alpha, \tag{2.4}$$

in which $\boldsymbol{E}(\boldsymbol{x}) = (\nabla\boldsymbol{u}(\boldsymbol{x}) + (\nabla\boldsymbol{u}(\boldsymbol{x}))^T)/2$ and $\boldsymbol{\Omega}(\boldsymbol{x}) = (\nabla\boldsymbol{u}(\boldsymbol{x}) - (\nabla\boldsymbol{u}(\boldsymbol{x}))^T)/2$ denote the disturbance rate of strain and rate of rotation tensors, respectively. Provided that the disturbance velocity $\boldsymbol{u}(\boldsymbol{x})$ and its gradient $\nabla\boldsymbol{u}(\boldsymbol{x})$ can be calculated at the centre of mass of each particle, we can determine the motion of the particles by time integration of the dynamic equations (2.2) and (2.4).

2.1.2. *Hydrodynamic interactions*

Far-field hydrodynamic interactions between the suspended particles are captured through the disturbance velocity field. If the suspension is dilute, the effect of a particle on the fluid is to first order a point force equal to the gravitational force $\boldsymbol{F}$ and applied at its centre of mass. The disturbance velocity can therefore be calculated as a solution of the Stokes equations:

$$-\mu\nabla^2\boldsymbol{u} + \nabla p = \boldsymbol{f}, \quad \nabla\cdot\boldsymbol{u} = 0, \tag{2.5}$$

with a body force equal to:

$$\boldsymbol{f}(\boldsymbol{x}) = \sum_{\alpha=1}^{N}\boldsymbol{F}\delta(\boldsymbol{x}-\boldsymbol{x}_\alpha), \tag{2.6}$$

where $\delta(\boldsymbol{x})$ is the three-dimensional Dirac delta function.

The solution of equation (2.5) in an infinite fluid is a sum of point-force singularities or Stokeslets:

$$\boldsymbol{u}(\boldsymbol{x}) = \frac{1}{8\pi\mu}\sum_{\alpha=1}^{N}\left(\frac{\boldsymbol{I}}{|\boldsymbol{x}-\boldsymbol{x}_\alpha|} + \frac{(\boldsymbol{x}-\boldsymbol{x}_\alpha)(\boldsymbol{x}-\boldsymbol{x}_\alpha)}{|\boldsymbol{x}-\boldsymbol{x}_\alpha|^3}\right)\cdot\boldsymbol{F}, \tag{2.7}$$

and the solution in a periodic domain is also known (Hasimoto 1959). Equation (2.7) and its periodic counterpart suffer from some limitations: the solution indeed grows unbounded near the centre of mass of the particles as a consequence of the point-force approximation which is an asymptotic result valid far from the particle surface. Furthermore, the calculation of this disturbance velocity at each particle location is an expensive operation, scaling with the square of the number of particles. Fast algorithms have been devised in the past to reduce the cost of this calculation (Sierou & Brady 2001; Saintillan *et al.* 2005), but were based on periodic boundary conditions and typically only allowed the simulation of a few hundred to a few thousand particles.

Here we present a method for the evaluation of the disturbance velocity which completely neglects close particle interactions by smoothing the disturbance field at short distances. The singularity in the point-force solution arises from the Dirac delta functions in the forcing term equation (2.6). Instead of calculating the exact flow field induced by these point singularities, we use a Cartesian grid and assign the point forces exerted by the particles on the fluid to the neighbouring mesh points $\boldsymbol{x}_i$:

$$\boldsymbol{f}(\boldsymbol{x}_i) = \sum_{\alpha=1}^{N}\boldsymbol{F}M(\boldsymbol{x}_i-\boldsymbol{x}_\alpha). \tag{2.8}$$

$M(\boldsymbol{x})$ is the assigment function and depends on the nature and the order of the interpolation method used. The choice of $M(\boldsymbol{x})$ is somewhat arbitrary, provided that it satisfies a few basic conditions. We require that the sum of $M(\boldsymbol{x}_i)$ over all the grid points be one for the total force to be conserved, and that M have spherical symmetry. M should also be small beyond a certain cutoff radius for the force to remain local; ideally (although not necessarily) M should have a compact support. A good class of functions satisfying these properties are Cardinal B-splines (Schoenberg 1973; Hockney & Eastwood 1981; Deserno & Holm 1997). Other choices are possible: Maxey and coworkers for instance in their somewhat similar force-coupling method use Gaussian interpolants, which do not have a compact support (Maxey & Patel 2001; Lomholt & Maxey 2003).

2.1.3. *Solution of the Stokes equations*

Equation (2.8) defines a body force field on the Cartesian grid and can be substituted into the Stokes equations, which are then solved numerically with appropriate boundary conditions. In this work, two types of boundary condition are considered. One of our objectives is to investigate the effects of solid boundaries, and to this end we follow the approach of Bergougnoux *et al.* (2003) and seek a solution of the Stokes equations satisfying a tangential flow boundary condition (i.e. 'slip', but no penetration) on the walls of the container. While this differs from the exact no-slip boundary condition for viscous flow, it allows for a very efficient solution while capturing some effects of the walls; in particular, the no-flux boundary condition at the bottom wall will lead to large-scale recirculation in the lateral direction and homogenization, both of which have been suggested as potential mechanisms for the decay of the fluctuations in sphere suspensions (Ladd 2002; Bergougnoux *et al.* 2003).

The effects of the tangential flow along the walls are investigated more precisely in the Appendix, where the present solution is compared to a more accurate solution satisfying the no-slip boundary condition on two of the sidewalls (Mucha *et al.* 2004); in particular, tangential flow along the walls is shown to result in slightly overestimated velocity fluctuations.

We first observe that $\boldsymbol{f}(\boldsymbol{x}) = f(\boldsymbol{x})\hat{\boldsymbol{z}}$, and transform the scalar-valued function $f(\boldsymbol{x})$ as follows using sine and cosine series:

$$f(\boldsymbol{x}) = \sum_{\boldsymbol{k}} \hat{f}(\boldsymbol{k}) \cos\left(\frac{\pi k_x x}{L_x}\right) \cos\left(\frac{\pi k_y y}{L_y}\right) \sin\left(\frac{\pi k_z z}{L_z}\right), \tag{2.9}$$

in which the wavevector $\boldsymbol{k}$ in an orthogonal lattice is defined as

$$\boldsymbol{k} = \frac{k_x}{L_x}\hat{\boldsymbol{x}} + \frac{k_y}{L_y}\hat{\boldsymbol{y}} + \frac{k_z}{L_z}\hat{\boldsymbol{z}}, \tag{2.10}$$

with k_x, k_y and k_z integers. We then seek a solution for the velocity written as:

$$\boldsymbol{u}(\boldsymbol{x}) = \sum_{\boldsymbol{k}} \hat{u}(\boldsymbol{k}) \times \begin{cases} \dfrac{k_x k_z}{L_x L_z} \sin\left(\dfrac{\pi k_x x}{L_x}\right) \cos\left(\dfrac{\pi k_y y}{L_y}\right) \cos\left(\dfrac{\pi k_z z}{L_z}\right), \\ \dfrac{k_y k_z}{L_y L_z} \cos\left(\dfrac{\pi k_x x}{L_x}\right) \sin\left(\dfrac{\pi k_y y}{L_y}\right) \cos\left(\dfrac{\pi k_z z}{L_z}\right), \\ -\left(\dfrac{k_x^2}{L_x^2} + \dfrac{k_y^2}{L_y^2}\right) \cos\left(\dfrac{\pi k_x x}{L_x}\right) \cos\left(\dfrac{\pi k_y y}{L_y}\right) \sin\left(\dfrac{\pi k_z z}{L_z}\right). \end{cases} \tag{2.11}$$

Equation (2.11) automatically satisfies continuity and the tangential flow boundary condition. Substituting equations (2.9) and (2.11) into the Stokes equations (2.5) allows us to solve for the Fourier coefficients of the velocity:

$$\hat{u}(\boldsymbol{k}) = \frac{\hat{f}(\boldsymbol{k})}{\pi^2 \left[\left(\dfrac{k_x}{L_x}\right)^2 + \left(\dfrac{k_y}{L_y}\right)^2 + \left(\dfrac{k_z}{L_z}\right)^2 \right]^2}. \tag{2.12}$$

The Fourier series expansions (2.9) and (2.11) can be truncated in each space dimension beyond a maximum wavenumber K_x, K_y, K_z, which should be chosen so as to make the shortest resolved wavelength shorter than the mean interparticle distance; the precise effects of the level of truncation are discussed in the Appendix. The velocity field and its gradient are then easily solved for using fast sine and cosine series algorithms.

For the sake of comparison we also consider periodic systems, and solve the Stokes equations spectrally. The velocity field is expanded as a Fourier series

$$\boldsymbol{u}(\boldsymbol{x}) = \sum_{\boldsymbol{k}} \hat{\boldsymbol{u}}(\boldsymbol{k}) \exp(-2\pi \mathrm{i} \boldsymbol{k} \cdot \boldsymbol{x}). \tag{2.13}$$

Hasimoto (1959) solved for the Fourier coefficients of the velocity:

$$\hat{\boldsymbol{u}}(\boldsymbol{k}) = -\frac{1}{4\pi^2 \mu \tau_0 k^2} \left(\boldsymbol{I} - \frac{\boldsymbol{k}\boldsymbol{k}}{k^2} \right) \cdot \hat{\boldsymbol{f}}(\boldsymbol{k}), \tag{2.14}$$

where $\hat{\boldsymbol{f}}(\boldsymbol{k})$ are the Fourier coefficients of the force distribution. As in the periodic case, the series are truncated at a finite number of terms, and the fast Fourier transform algorithm is used for good efficiency.

It should be noted that in the method described above, each particle feels its own disturbance, since the force field (equation (2.8)) used in the Stokes equations includes a contribution from the particle itself. Further adding this self-disturbance to the free-space sedimentation velocity $\boldsymbol{U}_s(\boldsymbol{p}_\alpha)$ in equation (2.2) would lead to a systematic overestimation of the sedimentation rates. In the simulations, the disturbance velocity $\boldsymbol{u}(\boldsymbol{x})$ felt by each particle was therefore corrected by subtracting this self-contribution, which can be calculated independently on the grid using a similar method.

In all of the following, distances are made dimensionless with the length $l_c = l$ of the major axis of a particle, velocities with the sedimentation speed $u_c = (\beta_0 + \beta_1)\Delta\rho V_p g/8\pi\mu l$ of an isolated vertical spheroid in an infinite fluid, and times with the time $t_c = l_c/u_c$ for an isolated vertical spheroid to sediment over the length of its major axis. In all simulations, third-order B-spline interpolation was used for the calculation of the body force field, and the number of Fourier modes was chosen so as to resolve the velocity field over distances of the order of half a particle length. The time integration was performed using a fourth-order Runge–Kutta scheme. For the most part, we treat the case of prolate spheroids ('fibres'), for which comparison with experimental data is possible; the case of oblate particles ('disks') is briefly addressed in § 2.7. Unless otherwise stated, the results shown are for non-periodic systems with slip boundary conditions.

2.2. *Particle distribution and concentration fluctuations*

Figure 1(*a*) shows a typical particle distribution, obtained for a simulation of 29 702 spheroids of aspect ratio $A = 15$ in a box of dimensions $L_x = 32$, $L_y = 12$, $L_z = 180$ (particle volume fraction $\phi = 0.1\%$). The initial condition is a homogeneous dispersion with random positions and orientations. As the sedimentation proceeds, a broad suspension front forms at the interface with the clear fluid and keeps growing in time. Careful observation of the bulk shows that the suspension does not remain homogeneous: particles instead tend to aggregate into clusters as predicted by Koch & Shaqfeh (1989). Particles are also observed to rotate and to orient preferentially in the vertical direction, with a strong correlation between centre-of-mass position and orientation; while the orientation remains random inside the dense clusters, the alignment in the vertical direction is much clearer in their periphery, where we will see that a strong vertical shear exists (e.g. § 2.4). We focus our analysis on the clustering phenomenon, and try to define measures for the concentration fluctuations in the bulk.

A good way of visualizing the inhomogeneities consists in considering the time trace over a short time interval of the smooth concentration field obtained by B-spline interpolation as explained in § 2.1.2:

$$\bar{c}(\boldsymbol{x}, t) = \frac{1}{\Delta t} \int_t^{t+\Delta t} \sum_{\alpha=1}^{N} M(\boldsymbol{x} - \boldsymbol{x}_\alpha(t')) \, \mathrm{d}t', \tag{2.15}$$

where a small value of the order of a few Stokes units is chosen for Δt ($\Delta t = 4$ in the results presented here). The advantage of this measure is that it allows us to visualize both the concentration fluctuations and the correlation in the motion of the particles. Figure 1(*b*) shows $\bar{c}(\boldsymbol{x}, t)$ in the vertical mid-plane $y = L_y/2$ at different times t over the course of the simulation of figure 1(*a*). In the initial instants, weak density fluctuations are present owing to the random nature of the initial distribution. A relatively strong flow is observed away from the walls at the centre of the cell, with recirculation vortices on the sides. This strong initial streamer spans the entire box

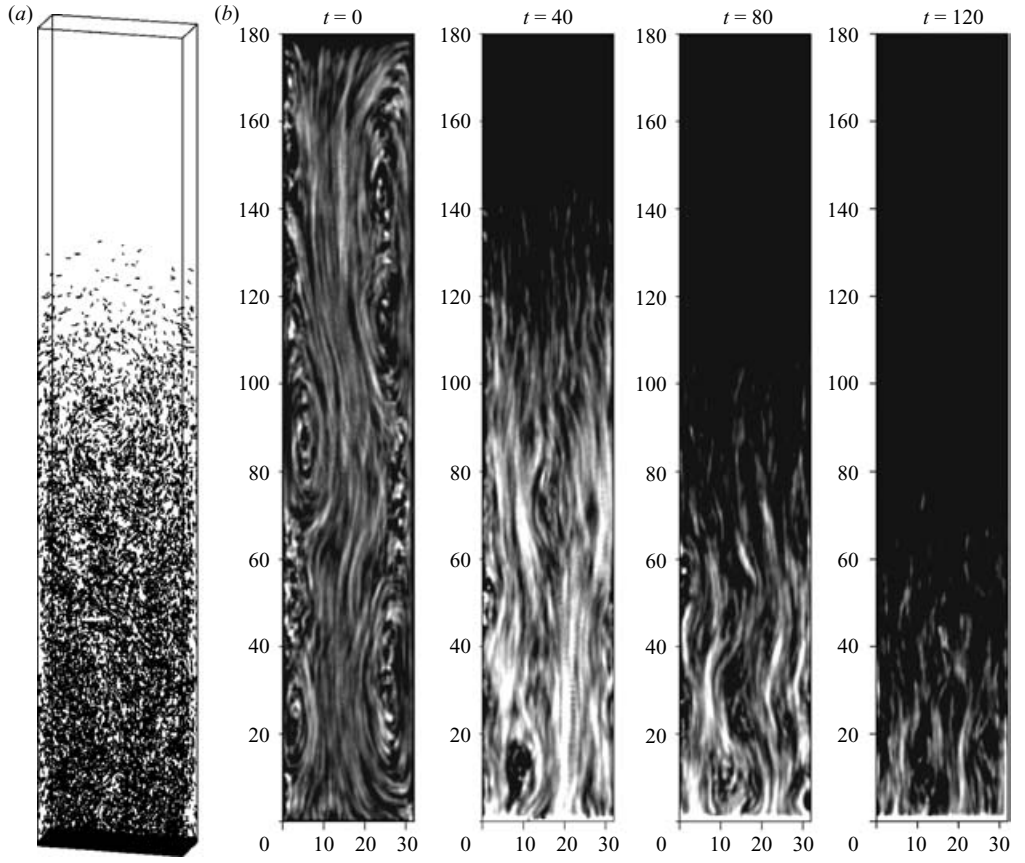

FIGURE 1. (*a*) Particle distribution at $t = 80$ for a simulation of 29 702 spheroids of aspect ratio $A = 15$ in a box of dimensions $L_x = 32$, $L_y = 12$, $L_z = 180$ (volume fraction $\phi = 0.1\%$). (*b*) Time trace of the concentration field over a short interval $\Delta t = 4$ in the mid-plane $y = L_y/2$, at various stages of the sedimentation (cf. equation (2.15)).

width, in agreement with the scaling of Hinch (1987), according to which velocity fluctuations in a random sedimenting suspension occur over length scales comparable to the width of the container. The streamer also spans the entire height of the box, in constrast to the circular vortical structures that are typically observed in sphere sedimentation (Guazzelli 2001); this very long autocorrelation in the vertical direction will be further explored in § 2.4. At later times ($t = 40$ to 80), this initial streamer is observed to break up into smaller structures; yet the concentration fluctuations intensify as a result of the Koch & Shaqfeh instability, leading to the formation of dense vertical streaks. Several streaks can be observed in the lateral direction (up to three or four at $t = 40$), suggesting that a wavenumber selection may be occurring. The inhomogeneities are found to persist up until the arrival of the sedimentation front, in spite of the decay of the velocity fluctuations in the fluid (see § 2.5). As the concentration in the suspension finally decreases owing to stratification (figure 3), the concentration fluctuations gradually become less intense ($t = 120$).

The fluctuations in the bulk can be measured more quantitatively by calculating the instantaneous Fourier transform of the concentration field over a section of the

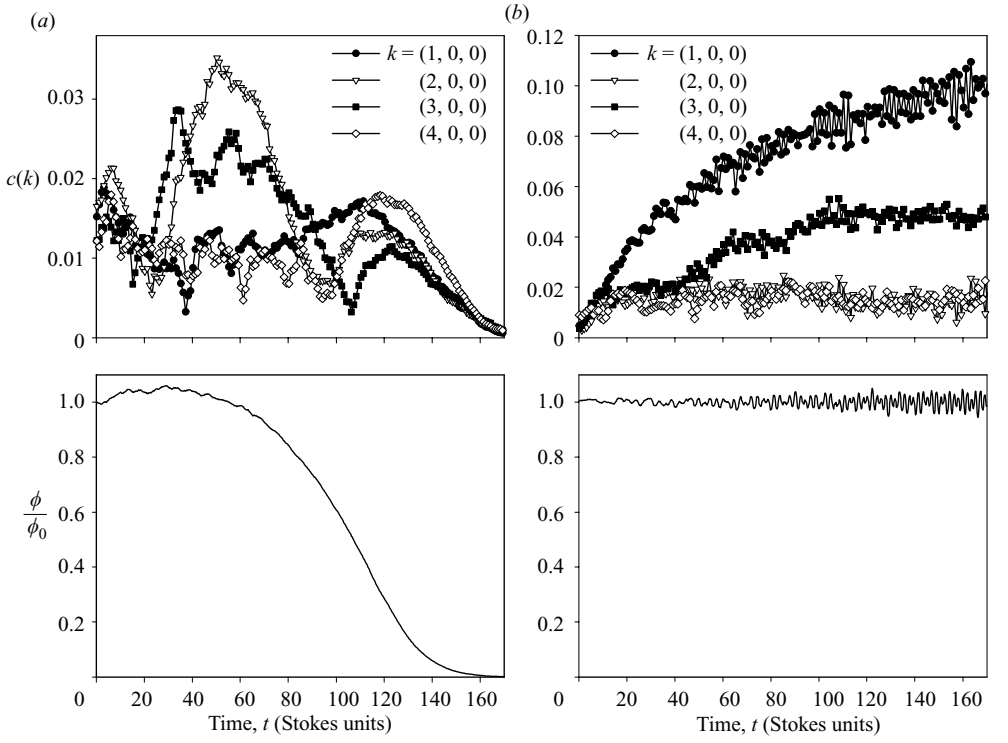

FIGURE 2. Time evolution of the Fourier coefficients of the concentration field for a simulation of 158 411 spheroids of aspect ratio $A = 15$ in a box of dimensions $L_x = 32$, $L_y = 32$, $L_z = 180$ (volume fraction $\phi = 0.2\%$), in both (*a*) non-periodic and (*b*) periodic boundary conditions. The spectra were calculated over a subsection of the container: $20 < z < 52$, and were averaged over four simulations. The lower plots show the evolution of the mean volume fraction in the section in which the spectra were obtained.

box:

$$\hat{c}(\boldsymbol{k}, t) = \int_{V'} c(\boldsymbol{x}, t) \exp(2\pi \mathrm{i} \boldsymbol{k} \cdot \boldsymbol{x}) \, \mathrm{d}\boldsymbol{x}. \tag{2.16}$$

In practice, $c(\boldsymbol{x}, t)$ is obtained by binning the particle positions, and $\hat{c}(\boldsymbol{k}, t)$ is calculated as a discrete Fourier transform. Figure 2 shows the time evolution of the magnitude of a few Fourier coefficients, obtained for a simulation in a box of dimensions $L_x = 32$, $L_y = 32$, $L_z = 180$ at a volume fraction of $\phi = 0.2\%$, in both non-periodic and periodic boundary conditions. In the periodic case (figure 2*b*), the longest wavelength in the horizontal direction $\boldsymbol{k} = (1, 0, 0)$ clearly dominates the spectrum, which corresponds to the formation of one main streamer (here each component of $\boldsymbol{k}$ is made dimensionless with the inverse size of the box in the corresponding direction). This is in agreement with the linear stability analysis of Koch & Shaqfeh (1989) which predicts that the shortest wavenumber (longest wave) should grow the fastest, and was also reported in previous simulations of periodic systems (Mackaplow & Shaqfeh 1998; Butler & Shaqfeh 2002; Saintillan *et al.* 2005). The behaviour is quite different in the non-periodic case (figure 2*a*), where the two wavevectors $\boldsymbol{k} = (2, 0, 0)$ and $\boldsymbol{k} = (3, 0, 0)$ are observed to grow and dominate the spectrum, corresponding to two or three dense streamers in the lateral direction. This is consistent with figure 1(*a*) where in a finite box several vertical streaks were shown to appear in the concentration field. After

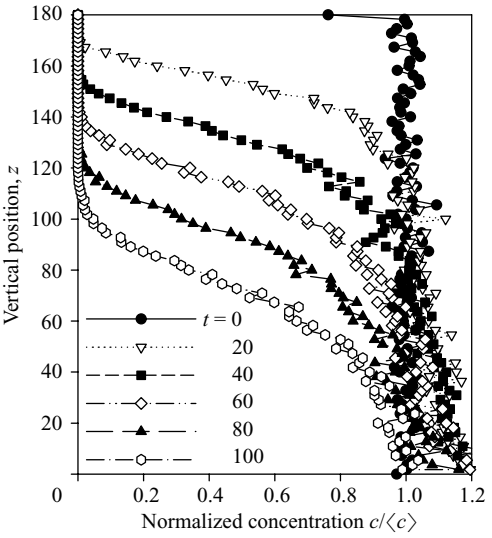

FIGURE 3. Cross-section averaged concentration profile in the vertical direction at various times during the sedimentation of a suspension of 148 510 spheroids of aspect ratio $A = 15$ in a box of dimensions $L_x = 32$, $L_y = 12$, $L_z = 180$ (volume fraction $\phi = 0.5\%$). The concentration profile is normalized by its average value $\langle c \rangle$.

about 100 time units, the arrival of the front leads to a decay of the fluctuations at all wavenumbers, whereas in the periodic case, the fluctuations keep growing and do not show any sign of saturation.

The stratification and fluctuations in the vertical direction are illustrated in figure 3, showing the time evolution of the concentration profile in the z-direction (where concentration has been averaged in the horizontal plane). Initially, the transition from the bulk concentration $c = \langle c \rangle$ to zero (clear fluid) is quite sharp. As time goes on, the dispersion in orientation and anisotropic mobility of the particles result in the broadening of the interface; this is demonstrated by the change in the slope of the profile inside the front, which indicates a much smoother transition. Such a smooth transition is not typically observed in suspensions of spherical particles where the interface remains quite sharp throughout the sedimentation process (see Bergougnoux *et al.* 2003 for instance, as well as figure 17*b*). Figure 3 also presents another interesting feature, as the concentration in the suspension and in particular near the bottom of the container is observed to exceed the mean bulk value $\langle c \rangle$. This constitutes another proof of clustering, and also suggests an additional mechanism for the broadening of the front, which may be due not only to the dispersion in orientation, but also to the segregation of the clusters near the bottom of the box, as particle aggregates have enhanced sedimentation speeds.

2.3. *Pair distribution function and structure factor*

The microstructural arrangement of the particles in the suspension is captured well by the pair distribution function, which is the distribution of pairs of particles at a given centre-of-mass to centre-of-mass distance (Ladd 1992). As observed in the previous section, the microstructure in the suspension is highly anisotropic; to confirm the arrangement of the spheroids into several vertical streamers in the horizontal

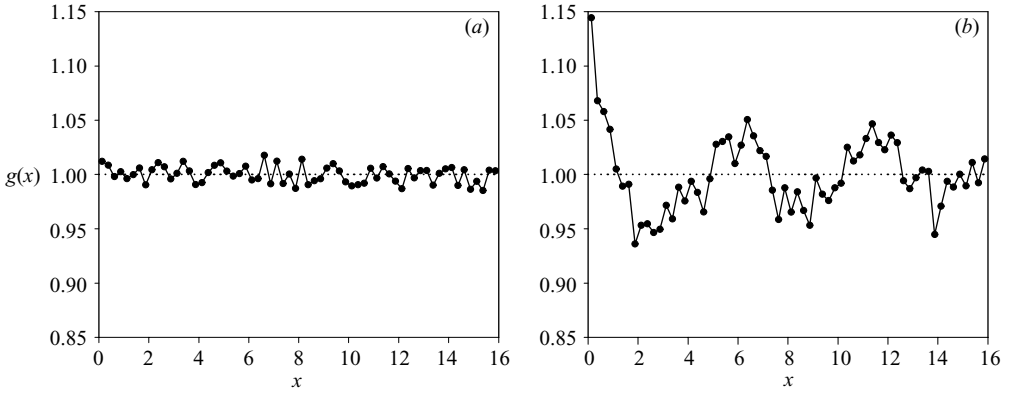

FIGURE 4. Pair distribution function in the lateral direction at (*a*) $t=0$ and (*b*) $t=100$ for a simulation of 29 952 spheroids of aspect ratio $A=15$ in a box of dimensions $L_x=32$, $L_y=12$, $L_z=180$ (volume fraction $\phi=0.1\%$). $g(x)$ was calculated over the subdomain $20<z<30$.

direction, we define a pair distribution function in the lateral direction:

$$g(x)=\frac{V}{N^2}\left\langle \sum_i \sum_{j\neq i} \delta(x-x_{ij}) \right\rangle, \tag{2.17}$$

where $x_{ij}=|x_i-x_j|$ is the separation distance along the x–axis between particles i and j, and $\langle\cdot\rangle$ denotes the ensemble average. To avoid artefacts due to the container sidewalls, the suspension is replicated periodically in the x-direction and the closest separation distance is used when calculating $g(x)$. Figure 4 shows the pair distribution function at $t=0$ and $t=100$ for a typical simulation. At $t=0$, $g(x)$ is essentially constant as the particle distribution is uniform; this is a consequence of our simulation model in which excluded volume interactions are completely neglected. $g(x)$ does not remain uniform however, as shown in figure 4(*b*). A peak near $x=0$ is observed to form; this maximum, which had been reported in previous studies (Butler & Shaqfeh 2002; Kuusela *et al.* 2003), is a sign of clustering and means that there is an excess of particles in the vicinity of any given particle. Oscillations also appear away from $x=0$, i.e. the arrangement of the particles does not remain uniform and random, but becomes structured at long wavelengths as a result of the formation of the streamers in the lateral direction.

The data from the pair distribution function are best analysed by taking the Fourier transform of their fluctuating part, yielding the structure factor:

$$S(k)=\int \exp(-2\pi \mathrm{i}kx/L_x)\,(g(x)-1)\,\mathrm{d}x. \tag{2.18}$$

The evolution of the structure factor for the same simulation as in figure 4 is shown in figure 5. At $t=0$, no particular frequency dominates the spectrum. Progressively a peak appears at $k=1$ and $k=2$ ($t\approx 40$), and slowly migrates towards $k=3$ while becoming more intense. The data are very well reproducible from one simulation to another for a given set of parameters, and this suggests that a wavenumber selection is indeed taking place. As shown in figure 5, the wavenumber selection is associated with the decay or breakup of the initial mode $k=1$, and is linked to the presence of container walls as it is not observed in periodic boundary conditions where the longest mode dominates throughout the simulation.

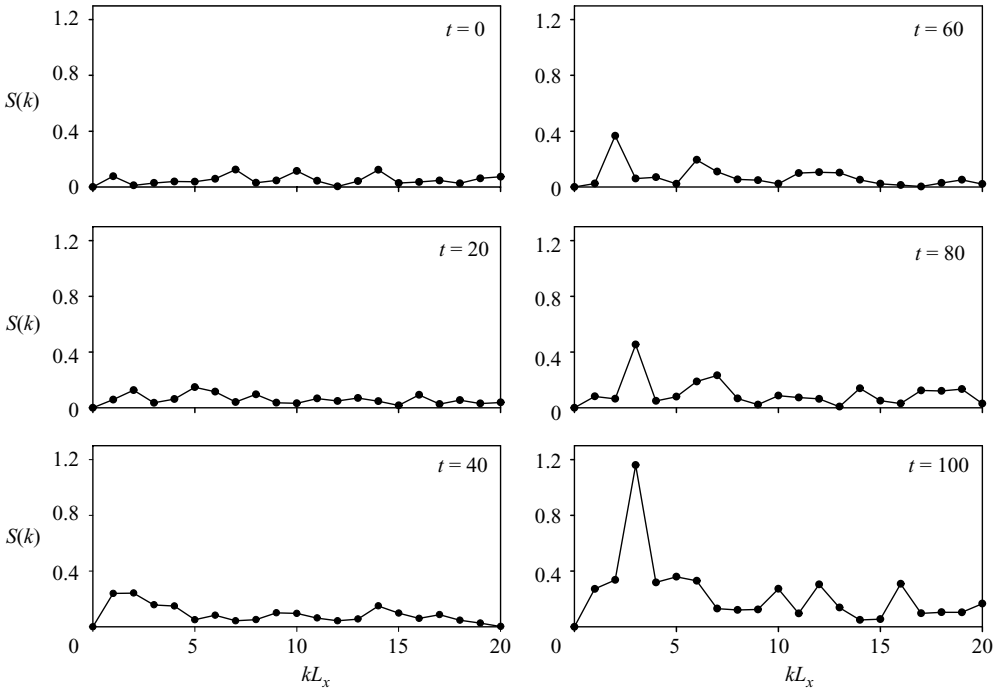

FIGURE 5. Time evolution of the structure factor for the simulation of figure 4 (29 952 spheroids, $A = 15$, $L_x = 32$, $L_y = 12$, $L_z = 180$, $\phi = 0.1\%$). The structure factor was obtained by taking the Fourier transform of the fluctuating part of the pair distribution $g(x)$ shown in figure 4 (equation (2.18)).

Box dimensions (L_x, L_y, L_z)	Final spacing between streamers
(16, 12, 180)	6.61
(32, 12, 180)	5.83
(48, 12, 180)	6.80
(64, 12, 180)	6.56
(32, 32, 180)	5.94

TABLE 1. Influence of the container dimensions on the wavenumber selection in suspensions of spheroids of aspect ratio $A = 15$ at a volume fraction of $\phi = 0.1\%$. The spacing between streamers is estimated using the position of the second peak that appears in the pair distribution function $g(x)$ (see figure 4). At given values of A and ϕ, the final wavelength of the fluctuations is insensitive to the size of the container.

The dependence of the final wavelength of the fluctuations on the dimensions of the container is investigated in table 1, where the final position of the second peak in the pair distribution function $g(x)$, which gives an estimate of the spacing between streamers, is shown for various box dimensions. At given values of the volume fraction and of the particle aspect ratio, the position of the peak is fairly insensitive to the lateral dimensions L_x and L_y of the simulation box; at $\phi = 0.1\%$ and $A = 15$, the data of table 1 give a spacing of approximately 6 particle lengths in the lateral direction. This confirms that the initial fluctuations over the width of the box give way to

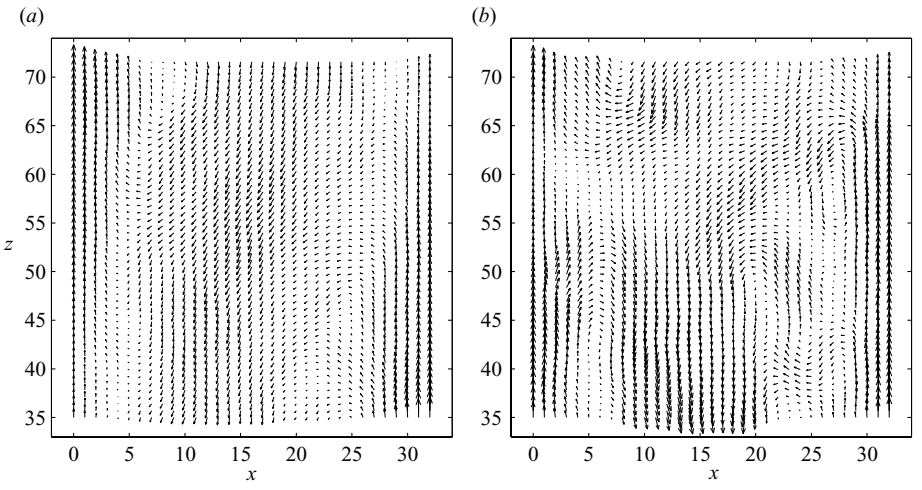

FIGURE 6. Velocity disturbance field at (*a*) $t=0$ and (*b*) $t=60$ in the midplane $y=L_y/2$, for a simulation of 59 904 spheroids of aspect ratio $A=15$ in a box of dimensions $L_x=32$, $L_y=12$, $L_z=180$ (volume fraction $\phi=0.2\%$).

fluctuations at a wavelength that does not depend on the container dimensions, and must therefore scale with the interparticle distance in the suspension. This transition from box-dependent to box-independent concentration fluctuations is analogous to what was previously reported for the velocity fluctuations in suspensions of rigid spheres (e.g. Nicolai and Guazzelli 1995; Guazzelli 2001), suggesting that similar mechanisms may be at play. Additional work is required to determine the precise scaling of the final wavelength with the mean interparticle distance (or equivalently the volume fraction) and with the aspect ratio of the spheroids.

2.4. *Velocity disturbance field*

The inhomogeneous microstructure described above is also visible from the velocity disturbance field. Typical velocity fields are shown in figure 6 at the beginning of the sedimentation and at a later time ($t=60$). At $t=0$, a strong flow is observed near the centre of the box with recirculation near the walls, in agreement with the observations made previously on the time trace of the concentration field (figure 1*b*). Note that the non-zero disturbance velocity at the walls is an artefact of the slip boundary condition used in the simulations, and would not be observed in an experiment. However, backflow near the walls can still be expected even in no-slip boundary conditions because of the depletion layer existing near the walls due to excluded volume, which has a characteristic thickness of the order of half a particle length (Mor *et al.* 2003). As already observed in figure 1(*b*), this initial flow spans most of the box height, unlike the stacking of circular cells that has been reported for spheres (e.g. Guazzelli 2001); this may be a consequence of the depletion layer, which is almost inexistent in sphere suspensions at the volume fractions considered here. Over the course of the sedimentation, smaller structures appear in the velocity field, as shown in figure 6(*b*) at $t=60$. The disturbance field now looks more chaotic, and presents distinct swirls over shorter lengths scales. The vortices are slightly stretched in the vertical direction, suggesting that the correlation is stronger in the direction of gravity.

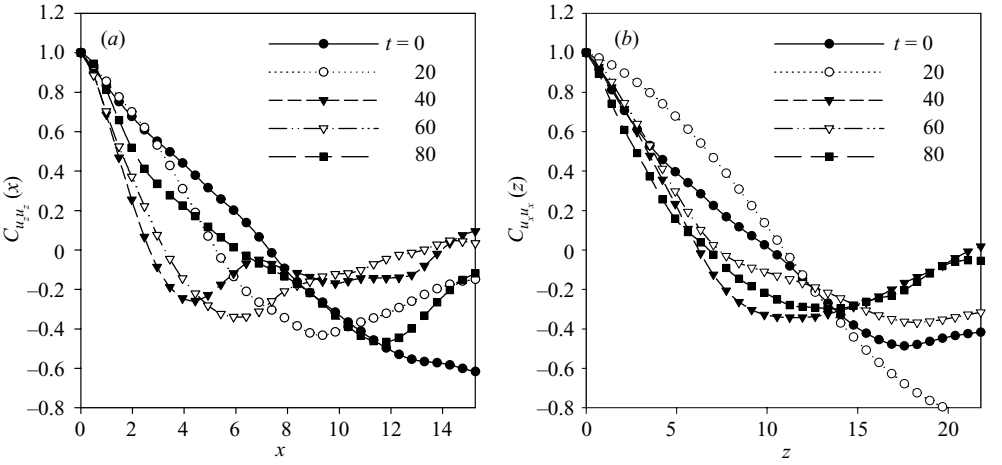

FIGURE 7. Time evolution of the autocorrelation function of: (*a*) the vertical velocity component in the lateral direction, and (*b*) the horizontal velocity component in the vertical direction. The results are for a simulation of 59 904 spheroids of aspect ratio $A = 15$ in a box of dimensions $L_x = 32$, $L_y = 12$, $L_z = 180$ (volume fraction $\phi = 0.2\%$).

These qualitative observations are confirmed in figure 7, which shows the evolution of the autocorrelation functions of the velocity field. Figure 7(*a*) shows the autocorrelation $C_{u_z u_z}(x)$ in the lateral direction x of the vertical velocity component u_z. At $t = 0$, the function decorrelates very slowly and reaches a minimum beyond $x = 15$ which is approximately half a box width: this very slow decay in the lateral direction was expected as a result of the aforementioned streamer spanning the entire box width at the beginning of sedimentation. Progressively, a clearer minimum appears and shifts towards lower values of x. At $t = 40$, the minimum near $x = 4$ corresponds to an anticorrelation in the vertical velocity field, i.e. to the presence of fluid streams flowing in opposite directions. A second peak is then observed again near $x = 7$. This negative correlation followed by an increase in the correlation is indicative of a succession of similar vortex structures in the lateral direction, corresponding to the clusters or streamers observed in the particle distribution. In particular, the position of the peak $x = 7$ can be used as a rough estimate of the spacing between the clusters; in a box of width $L_x = 32$ this corresponds to approximately four structures, which is in relatively good agreement with the wavenumber obtained from the structure factor. Note that after a while ($t = 80$ and beyond), the position of the minimum in the correlation function starts increasing again as a result of the arrival of the sedimentation front, and of the very strong damping of all the fluctuations in the fluid.

Figure 7(*b*) shows the autocorrelation $C_{u_x u_x}(z)$ in the vertical direction z of the horizontal velocity component u_x. The behaviour is somewhat similar; starting from a very long correlation length (of the order of 15 to 20 particle lengths), the position of the minimum shifts to a lower value $z \approx 10$. This value, however, remains substantially greater than the shortest length of 4 observed in the lateral direction. This confirms that the structures in the velocity field and the particle distribution are stretched in the vertical direction, typically by a factor greater than two.

The evolution of the disturbance field is reminiscent of observations made previously on sphere suspensions (e.g. Segrè *et al.* 1997; Guazzelli 2001; Tee *et al.* 2002). In the case of spheres, the initial disturbance field is characterized by large recirculation

cells induced by the random Poisson statistics due to the initial mixing; these cells are then observed to break up into smaller swirls, whose characteristic size in most experiments is found to be of the order of 15 interparticle distances, and therefore does not depend on the container dimensions. Several mechanisms have been proposed for the decay of the correlation length and of the fluctuations as reviewed in § 1. The clear analogy with the results reported here suggests that the same mechanisms leading to the decay of velocity fluctuations in sphere suspensions may play a role in the wavenumber selection process observed in our simulations. In particular, the initial strong convection current may be decaying as a result of homogenization at long wavelengths before the strongest mode ($k = 1$) of the instability has any time to grow significantly. The strong stratification illustrated in figure 3 can also be expected to play an important part (in fact much more important than for spheres because of the dispersion in orientation which acts like a polydispersity), and may be responsible for the continuous decay of the velocity fluctuations with no steady state as discussed in § 2.5. Despite the qualitative similarities, the previous discussion also casts light on several important differences. While the decay of the velocity correlation length in sphere sedimentation is accompanied by, and possibly a result of, the homogenization of the particle distribution in the horizontal direction (Lei *et al.* 2001; Nguyen & Ladd 2004, 2005), homogenization occurs only down to the wavelength of the instability in the case of spheroids; quite strong density fluctuations persist between the core of the streamers and the clarified fluid, as discussed in § 2.2. A detailed comparison of the length scales of the fluctuations in both situations would be worthwhile in order to fully appreciate the effects of the instability. As a result of the clustering, the velocity field in the case of spheroids also maintains a much stronger correlation in the vertical direction: long streamers of dense fluid alternate with clarified regions of backflow, unlike the circular swirls induced by the much weaker density fluctuations in sphere suspensions.

2.5. *Velocity statistics*

The effects of the instability on the sedimentation velocity are twofold. As will be discussed in § 2.6, the strong vertical shear between the dense and clarified regions causes the spheroids to orient vertically, resulting in an increase of their individual sedimentation speed. Moreover, the arrangement of the particles into dense clusters allows for the clusters to sediment faster, which can be viewed as a shielding effect. The combination of these two effects can result in sedimentation velocities that exceed the maximum velocity for an isolated particle, as illustrated in figure 8 where the velocities are made dimensionless by the velocity of a single vertically oriented spheroid. Figure 8(*a*) shows the evolution of the mean sedimentation velocity at various volume fractions. Starting from an initial value close to the sedimentation rate of 0.83 for spheroids of aspect ratio of $A = 15$ at infinite dilution, the mean sedimentation velocity rapidly increases to reach a maximum value ranging from 1.5 in the more dilute case ($\phi = 0.1\%$) to approximately 1.6 at $\phi = 0.5\%$. After this strong peak, the mean velocity decays slowly back towards smaller values, until the arrival of the front in which the velocities are found to be much weaker. The curves do not present any steady state, i.e. the particle velocity at a given vertical station varies continually; the mean velocity is also observed to depend slightly on the height at which it is measured. This differs from the experimental observations of Herzhaft & Guazzelli (1999), who reported a mean velocity steady state; this may be a consequence of the limited height of the box in our simulations, or of the approximate boundary conditions on the sidewalls. Herzhaft & Guazzelli (1999)

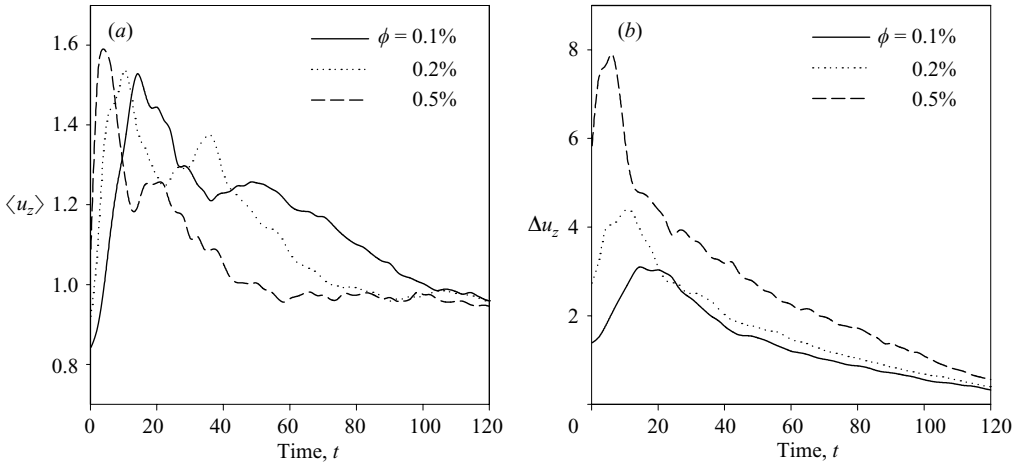

FIGURE 8. (*a*) Mean sedimentation velocity $\langle u_z \rangle$, and (*b*) mean velocity variance in the z–direction Δu_z at various volume fractions. The results are for spheroids of aspect ratio $A = 15$ in a box of dimensions $L_x = 32$, $L_y = 12$, $L_z = 180$. The results were obtained in a subsection of the box: $45 < z < 67.5$, and are averaged over ten simulations to remove statistical fluctuations.

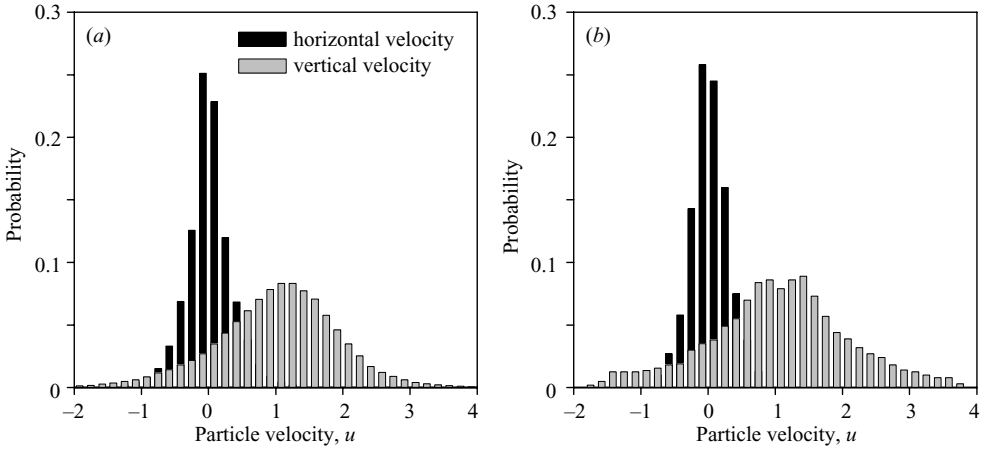

FIGURE 9. Velocity distributions obtained from: (*a*) simulations, and (*b*) the experiments of Herzhaft & Guazzelli (1999). The simulation results are for a suspension of 41 530 spheroids of aspect ratio $A = 11$ in a box of dimensions $L_x = 32$, $L_y = 12$, $L_z = 180$ (volume fraction $\phi = 0.26\%$); the distribution shown was obtained shortly after the peak of the mean velocity (cf. figure 8). The experimental distribution of Herzhaft & Guazzelli was obtained in a suspension of cylindrical fibres of aspect ratio $A = 11 \pm 2$, at a volume fraction of $\phi = 0.26 \pm 0.01$ %.

observed an increase of the mean sedimentation speed with concentration in the dilute regime, in agreement with our results. The values they report for the mean velocity are (for cylindrical fibres of aspect ratio $A = 11 \pm 2$): 1.1 ± 0.2 at $\phi = 0.1\%$ and 0.26%, and 1.5 ± 0.3 at $\phi = 0.48\%$, which fall slightly below the peak values shown in figure 8(*a*), but are of the same order as the simulated velocities after the initial peak.

A more precise comparison to the experiments of Herzhaft & Guazzelli (1999) is shown in figure 9, which compares the distributions of the vertical and horizontal

velocity components from our simulations with the experimental measurements at $\phi \approx 0.26\%$. Because no steady state is observed as noted previously, the velocity distribution evolves with time. The choice of a specific time to calculate the distributions is therefore *ad hoc*; figure 9(*a*) shows the distribution measured after the initial velocity peak, when the initial box-dependent streamer has started to decay and when the concentration fluctuations have had time to develop. The two distributions show very good qualitative and quantitative agreement. As already mentioned, the mean sedimentation speed and variance are very slightly overestimated in the simulations. However, it should be emphasized that the agreement with the experimental results is significantly better than that previously obtained in periodic boundary conditions (Butler & Shaqfeh 2002; Saintillan *et al.* 2005), where a strong dependence on the system size and box aspect ratio was found, and where both the mean and variance of the vertical velocity were strongly overpredicted.

Figure 8(*b*) shows the evolution of the velocity fluctuations in the suspension. The fluctuations are found to be very strong shortly after the start of sedimentation (sensibly at the same time as the velocity peak), reaching values of up to four times the mean velocity for $\phi = 0.5\%$; very high values for the fluctuations had also been reported by Herzhaft & Guazzelli (1999). These fluctuations are partly caused by the strong initial flow at the centre of the box, which is accompanied by an equally strong backflow near the walls. Shortly after reaching their maximum value, the fluctuations are then observed to decay rapidly towards zero; again no steady state is observed. The steady decay of the fluctuations after the initial peak is similar to what is observed for spheres (e.g. Nicolai *et al.* 1995; Ladd 2002; Tee *et al.* 2002; Bergougnoux *et al.* 2003; Mucha *et al.* 2004). While in the case of spheres, steady velocity fluctuations are reached in some cases, they have also been predicted to decay *ad infinitum* in suspensions in which stratification is significant (Luke 2000; Mucha & Brenner 2003). Stratification being very strong in anisotropic suspensions such as those of this study, it most probably plays a role in the damping of the velocity variance shown in figure 8(*b*).

Note that inaccuraries in the particle velocities and velocity fluctuations can be expected given our simulation method. Most importantly, the zero tangential stress boundary condition on the sidewalls differs significantly from the exact no-slip boundary condition for viscous flow, with possible consequences on the rate of decay of hydrodynamic interactions. This was pointed out by Brenner (1999), who investigated the effects of sidewalls on fluctuations in sedimenting sphere suspensions and showed that the no-slip boundary condition results in a screening of interactions beyond a few wall separation distances. While enforcing the correct boundary condition on all container walls is difficult, we also implemented the Green's function of Mucha *et al.* (2004) which satisfies no-slip on two of the sidewalls. The results, which are described in more detail in the Appendix, indeed show that tangential flow on the sidewalls leads to a systematic overestimation of the velocity fluctuations (as well as the mean velocity, albeit to a lesser extent). The velocity fluctuations in a real system are therefore likely to be weaker than those shown in figure 8(*b*), which is indeed the case for the values reported by Herzhaft & Guazzelli (1999). Yet the qualitative behaviour of the fluctuations (sharp increase followed by a steady decrease) is likely to be captured correctly. Other sources of inaccuracies may come from the substitution of a finite B-spline for the original point force at the centre of the particles, which introduces an error by smoothing the velocity disturbance field at high wavenumbers, and from the point-force model that completely neglects higher force moments on the particles such as stresslets, which are

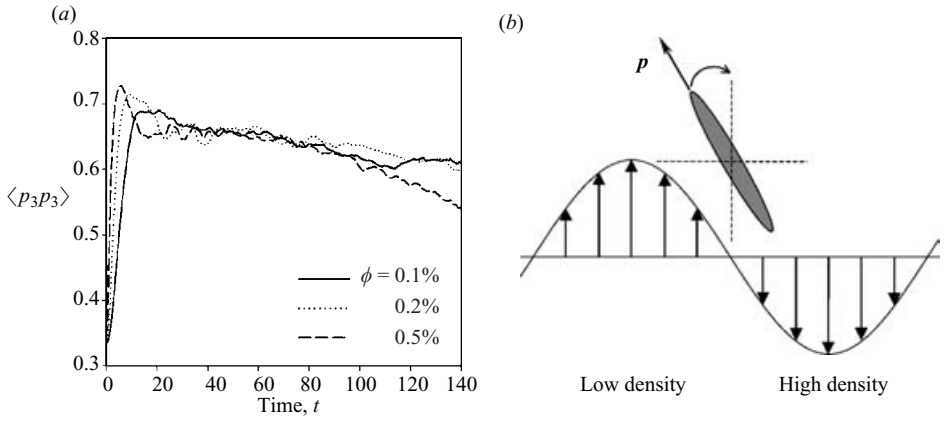

FIGURE 10. (*a*) Time evolution of the mean squared orientation in the direction of gravity $\langle p_3 p_3 \rangle$, at various volume fractions. The results are for spheroids of aspect ratio $A = 15$ in a box of dimensions $L_x = 32$, $L_y = 12$, $L_z = 180$. The results were obtained in a subsection of the box: $67.5 < z < 90$, and are averaged over ten simulations. (*b*) Diagram showing the mechanism for the orientation of a prolate spheroid along the vertical axis (after Koch & Shaqfeh (1989)).

responsible for the velocity hindrance observed in suspensions of spheres (Batchelor 1972).

2.6. *Orientation statistics*

Figure 10(*a*) shows the time evolution of the mean-squared orientation $\langle p_3 p_3 \rangle$ in the direction of gravity, which is a measure of the degree of alignment of the suspension in the vertical direction. The initial value of 1/3 corresponds to the isotropic orientation distribution in the initial configuration. Immediately after the start of sedimentation, $\langle p_3 p_3 \rangle$ increases sharply to reach a peak value of approximately 0.7, i.e. a very large number of spheroids quickly orient in the direction of gravity (figure 10*b*). As already mentioned earlier, this is a consequence of the strong vertical shear between the streamer at the centre of the box and the backflow near the walls. The fastest increase and the highest peak value are obtained in the more dense suspensions ($\phi = 0.5\%$), as a result of the stronger velocity fluctuations (figure 8*b*). After the peak is reached, $\langle p_3 p_3 \rangle$ very slowly and steadily decreases as fluctuations decay; its value remains however above 0.6 for the remainder of the simulation, suggesting that the alignment remains strong. After the initial peak, the value of $\langle p_3 p_3 \rangle$ is nearly the same for all volume fractions considered, even though the velocity fluctuations are typically stronger in more concentrated suspensions. This observation, however unexpected, was also made previously by Herzhaft & Guazzelli (1999), who found that the orientation distributions from their experiments were nearly identical at all concentrations.

A typical distribution of the projected angle (i.e. the angle made by the projection of the orientation vector $\boldsymbol{p}$ onto the (x, z)-plane with respect to the x-direction) is shown in figure 11 and compared to the experimental distribution of Herzhaft & Guazzelli (1999). The strong peak near 90° confirms the vertical alignment of many of the particles in the suspension. While the agreement between the two distributions is qualitatively fair, the peak is slightly underestimated in the simulations. The experimental distribution also presents a second peak near zero (corresponding to a horizontal alignment), whose origin is not clear and which is not captured in the simulations. Close particle interactions, which are completely neglected in

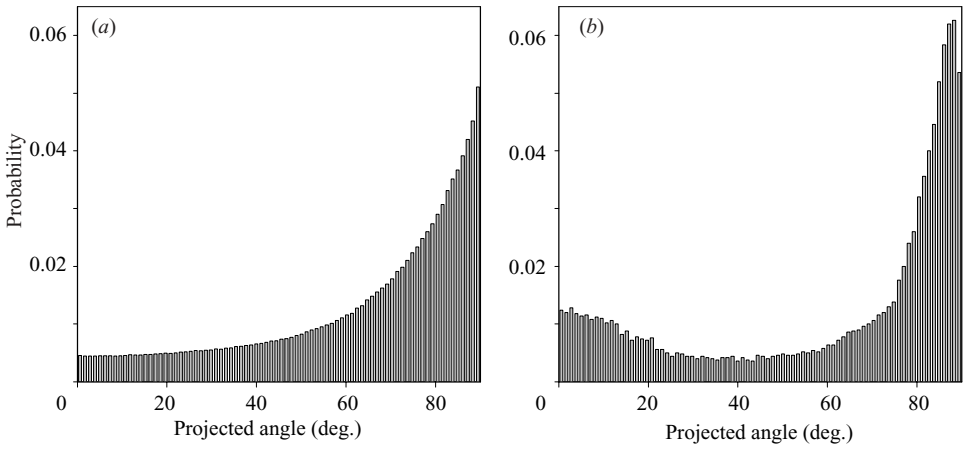

FIGURE 11. Distributions of the projected angle (angle of the projection of the orientation vector of the particles onto a vertical plane with respect to the horizontal) obtained from: (*a*) simulations, and (*b*) the experiments of Herzhaft & Guazzelli (1999). The simulation results are for a suspension of 41 530 spheroids of aspect ratio $A = 11$ in a box of dimensions $L_x = 32$, $L_y = 12$, $L_z = 180$ (volume fraction $\phi = 0.26\%$); the distribution shown was obtained shortly after the peak of the mean squared orientation $\langle p_3 p_3 \rangle$ (cf. figure 10). The experimental distribution of Herzhaft & Guazzelli was obtained in a suspension of cylindrical fibres of aspect ratio $A = 11 \pm 2$, at a volume fraction of $\phi = 0.26 \pm 0.01\%$.

our simulations, may slightly influence the shape of the distribution: the strong entanglements inside the clusters due to excluded volume may indeed have an effect on the orientation of the particles. Yet the second minimum in the experimental distribution must have another origin, as it was not reproduced either in the previous simulations by Butler & Shaqfeh (2002) and Saintillan *et al.* (2005). These also underpredicted the height of the main peak in most cases. The present simulations offer the improvement that the distribution does not significantly depend on the size or the aspect ratio of the sedimenting system. Future work will focus on including close interactions such as excluded volume with the hope of obtaining a more quantitative agreement for the orientation distributions.

2.7. *Oblate particles*

The previous discussion has focused entirely on prolate spheroids ($A > 1$), for which experimental data are available. The case of oblate spheroids ($A < 1$), or disk-shaped particles, has received less attention in the past in spite of its common occurrence in environmental fluid mechanics for instance, where the sedimentation of clay is a relevant example. To our knowledge, the concentration instability has never been studied either experimentally or numerically for oblate particles since its theoretical prediction by Koch & Shaqfeh (1989).

Simulations were run for oblate spheroids of aspect ratio $A = 0.3$ at various volume fractions. The results were found to be qualitatively similar to those discussed above for prolate particles, and only the main differences are summarized here. As in the case of prolate particles, inhomogeneities are observed to develop in the suspension. This clustering is again accompanied by an enhancement of the mean sedimentation rate. Figure 12(*a*) shows the evolution of the mean velocity in the suspension at two different volume fractions. The velocities are scaled by the sedimentation velocity of a particle whose major axis points in the vertical direction (the slowest configuration for an oblate spheroid), hence a lower bound of 1 for the velocity. Starting from a

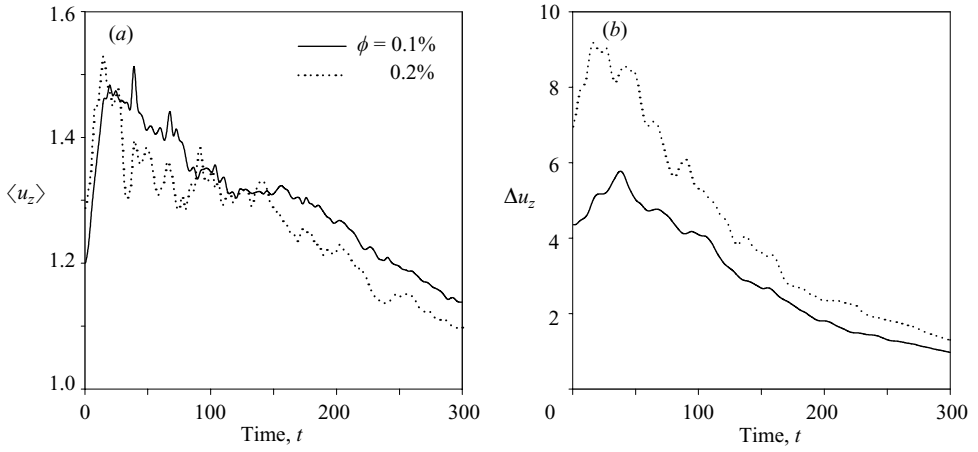

FIGURE 12. (*a*) Mean sedimentation velocity $\langle u_z \rangle$, and (*b*) mean velocity variance in the z-direction Δu_z at various volume fractions. The results are for oblate spheroids of aspect ratio $A = 0.3$ in a box of dimensions $L_x = 130$, $L_y = 40$, $L_z = 750$. The results were obtained in a subsection of the box: $187 < z < 281$, and are averaged over ten runs.

value between 1.2 and 1.3 (compared to the expected value of 1.12 for spheroids of aspect ratio $A = 0.3$ at infinite dilution), the sedimentation velocity quickly increases and reaches a peak value around 1.5 at both $\phi = 0.1\%$ and 0.2%. Figure 12(*b*) shows the corresponding velocity fluctuations, which are found to be about twice as strong as in the prolate case at the same concentrations (figure 8b). This can be explained as follows: oblate particles have a weaker mobility (because of their larger surface to volume ratio). At equivalent volume fraction they create the same fluctuations as prolate particles, but sediment more slowly; when scaled by the mean sedimentation speed, the fluctuations therefore appear much stronger. Note again that these fluctuations are also likely to be overestimated as a result of the zero tangential stress boundary condition at the sidewalls.

The enhancement of the velocity (figure 8*a*), as well as the concentration fluctuations (not shown), are found to be somewhat weaker than in the prolate case. A possible explanation is that the very strong velocity fluctuations observed above cause a more rapid alignment of the particles in the disturbance flow, which then hinders their lateral migration. Another likely reason is that the fluctuations result in more mixing, which limits the growth of the inhomogeneities. The strong alignment of the particles is illustrated in figure 13(*a*), which shows the mean-squared orientation $\langle p_3 p_3 \rangle$ in the direction of gravity. Note that in the case of oblate particles, the alignment occurs in such a way that the orientation vector $\boldsymbol{p}$ of the major axis points in a horizontal direction (figure 13*b*). As shown in figure 13(*a*), the mean orientation very quickly reaches a steady state, and remains constant until the arrival of the suspension front.

3. Deformable particles

3.1. *Theoretical analysis*

In this section, we develop a model for suspensions of deformable particles under sedimentation and investigate the stability of the suspension to fluctuations in concentration. As will become apparent, the formalism is similar to that developed by Koch & Shaqfeh (1989) for suspensions of spheroids, although significant differences

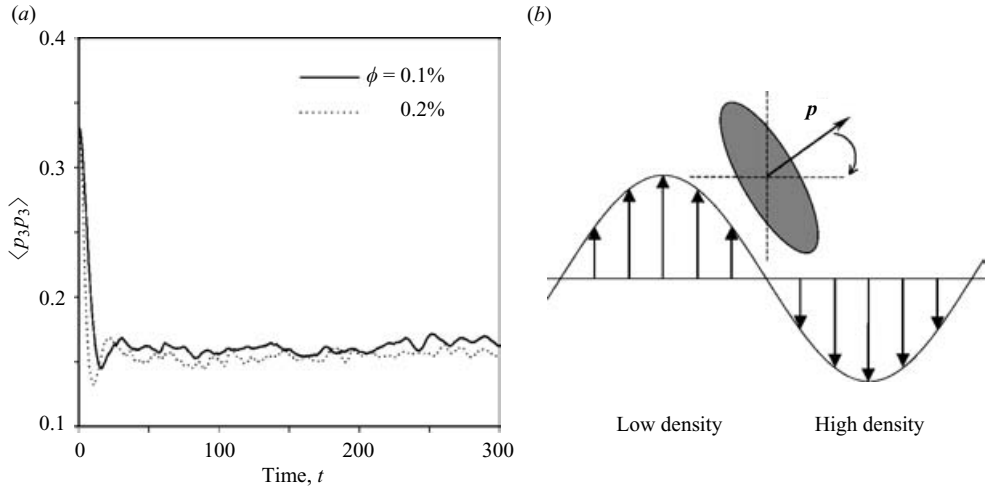

FIGURE 13. (*a*) Time evolution of the mean squared orientation in the direction of gravity $\langle p_3 p_3 \rangle$, at various volume fractions. The results are for oblate spheroids of aspect ratio $A = 0.3$ in a box of dimensions $L_x = 130$, $L_y = 40$, $L_z = 750$. The results were obtained in a subsection of the box: $94 < z < 187$, and are averaged over ten runs. (*b*) Diagram showing the mechanism for the orientation dynamics: in the case of oblate spheroids the orientation vector $\boldsymbol{p}$ aligns in a horizontal direction (after Koch & Shaqfeh (1989)).

exist. We first explain the micromechanical model used to describe the particle deformations and hydrodynamic interactions in § 3.1.1, then define a convective–diffusive equation for the concentration field in a suspension of such particles in § 3.1.2, and perform a linear stability analysis based on this continuum model in § 3.1.3.

3.1.1. *Micromechanical model*

The particles we consider here are isotropic in the absence of flow, and by deformation we mean departure from isotropy. In particular, the particles need not be technically spherical, and we will explain in § 3.2 that the arguments developed here can apply for instance to flexible polymers with strong internal Brownian motion. We make the fundamental assumption that particle deformations remain small, and are entirely determined by the local rate of strain $\boldsymbol{E} = (\nabla \boldsymbol{u} + (\nabla \boldsymbol{u})^T)/2$ with no regard for the history of the flow and of particle position. This implicitly assumes that the particle shape adjusts instantaneously on the flow time scale, or, in other words, that the characteristic time for the shape relaxation (which is determined by properties such as surface tension for a drop, membrane elasticity for a capsule, or internal Brownian motion for a flexible polymer) is much less than the characteristic time scale of the flow (which is set by the balance between the gravity force on the density fluctuations and viscous dissipation); this condition will be justified and made more quantitative in § 3.2. Under this assumption, the mobility $\boldsymbol{M}(\boldsymbol{E})$ of a particle can be expanded in a Taylor series with respect to the undeformed configuration, leading to the following approximation:

$$\boldsymbol{M}(\boldsymbol{E}) \approx M_0(\boldsymbol{I} + \tau_s \boldsymbol{E} + \cdots), \tag{3.1}$$

where $M_0 \boldsymbol{I}$ is the (isotropic) mobility of the undeformed particle, and τ_s is a characteristic time defining the response of the mobility to a weak flow field and

is a property of the particle. The condition on the flow strength can be written as:

$$\epsilon = \tau_s \dot{\gamma} \ll 1, \tag{3.2}$$

where $\dot{\gamma}$ is the effective characteristic shear rate of the disturbance flow imposed by the density fluctuations.

The centre-of-mass velocity $\boldsymbol{U}_\alpha$ of a particle α located at position $\boldsymbol{x}_\alpha$ in a suspension is then given by the sum of the sedimentation velocity of the particle and of the disturbance velocity in the fluid induced by the motion of the other particles:

$$\boldsymbol{U}_\alpha = \boldsymbol{U}_s + \boldsymbol{u}(\boldsymbol{x}_\alpha). \tag{3.3}$$

The sedimentation velocity can be written as $\boldsymbol{U}_s = \boldsymbol{M}(\boldsymbol{E}) \cdot \boldsymbol{F}$, where $\boldsymbol{M}(\boldsymbol{E})$ is given by equation (3.1) evaluated at position $\boldsymbol{x}_\alpha$, and $\boldsymbol{F} = \Delta\rho V_p \boldsymbol{g}$ is the gravity force on the particle. To leading order, the disturbance velocity $\boldsymbol{u}$ induced by the other particles in the suspension satisfies the Stokes equations:

$$-\mu\nabla^2\boldsymbol{u} + \nabla p = \boldsymbol{F}\sum_{\beta\neq\alpha}\delta(\boldsymbol{x}_\beta - \boldsymbol{x}), \quad \nabla\cdot\boldsymbol{u} = 0, \tag{3.4}$$

where $\delta(\boldsymbol{x})$ is the three-dimensional Dirac delta function, and the sum is over all particles in the suspension other than α. The only disturbance of a given particle on the fluid is therefore taken to be a point force, which is a valid approximation if the suspension is dilute. In a more accurate model, higher force moments (stresslets etc.) would have to be taken into account.

3.1.2. *Continuum limit*

Based on the above model for particle deformations, a conservation equation can be written for the evolution of the concentration of particles in a suspension. Under the assumption discussed previously on the instantaneous relaxation of particle configurations, only one particle shape can exist at a given position and at a given time, which allows us to define the variable $c(\boldsymbol{x}, t)$ as the concentration of particles at position $\boldsymbol{x}$ at time t. More precisely, the number of particles in an infinitesimal volume $\mathrm{d}\boldsymbol{x}$ surrounding the point $\boldsymbol{x}$ is given by $c(\boldsymbol{x}, t)\mathrm{d}\boldsymbol{x}$. $c(\boldsymbol{x}, t)$ is normalized by setting its mean value over the entire domain equal to the average number density n:

$$\frac{1}{V}\int_V c(\boldsymbol{x}, t)\,\mathrm{d}\boldsymbol{x} = n. \tag{3.5}$$

Using a different normalization, $c(\boldsymbol{x}, t)$ can also be interpreted as the probability density of finding a particle at position $\boldsymbol{x}$ and time t. $c(\boldsymbol{x}, t)$ satisfies the following conservation equation:

$$\frac{\partial c}{\partial t} + \nabla\cdot(\boldsymbol{U}c) - \nabla\cdot(\boldsymbol{D}\nabla c) = 0, \tag{3.6}$$

in which the rate of change of concentration at a given point is balanced by convective and diffusive fluxes. $\boldsymbol{U}$ is the centre-of-mass velocity of a particle at position $\boldsymbol{x}$, and is again given by equation (3.3). The disturbance velocity $\boldsymbol{u}$ now satisfies a continuum equivalent of equation (3.4), in which we include a body force proportional to the local number density:

$$-\mu\nabla^2\boldsymbol{u} + \nabla p = \boldsymbol{F}c(\boldsymbol{x}, t), \quad \nabla\cdot\boldsymbol{u} = 0. \tag{3.7}$$

The diffusion term in the conservation equation may have several origins. If the particles are small enough, Brownian diffusion will arise from the thermal fluctuations

in the solvent, leading to a diffusivity tensor given by the Stokes–Einstein relation: $\boldsymbol{D} = kT\boldsymbol{M}$, which may be anisotropic as the particles are allowed to deform. For the time being, we will assume that the centre-of-mass diffusion due to Brownian motion is negligible. Even in the absence of Brownian diffusion, hydrodynamic dispersion due to the random fluctuations in the disturbance velocity field will result in an effective diffusivity (e.g. Ham & Homsy 1988; Koch 1994; Nicolai *et al.* 1995), which is unknown *a priori* and is difficult to predict as it may evolve during the settling of the suspension. The details of this process are discussed more precisely in § 3.7, where our simulation results indeed show proof of a diffusive motion at long times. In general, it is fair to assume that the hydrodynamic diffusivity is anisotropic and can be written in the general form:

$$\boldsymbol{D} = D_{\parallel}\hat{\boldsymbol{z}}\hat{\boldsymbol{z}} + D_{\perp}(\boldsymbol{I} - \hat{\boldsymbol{z}}\hat{\boldsymbol{z}}), \tag{3.8}$$

where $D_{\parallel}$ and $D_{\perp}$ denote the diffusivities in the directions parallel to and perpendicular to gravity, respectively, and $\hat{\boldsymbol{z}}$ is a unit vector in the vertical direction.

3.1.3. *Linear stability analysis*

We now have all the ingredients to perform a linear stability analysis. The base state of the system corresponds to the absence of density fluctuations: $c(\boldsymbol{x}, t) = c_0$, in which case the disturbance velocity is zero everywhere ($\boldsymbol{u}(\boldsymbol{x}) = 0$), the particles are all isotropic, and a mean pressure gradient in the vertical direction balances the gravity force on the suspension: $\nabla p = \boldsymbol{F}c_0$. Consider now a small perturbation in particle density:

$$c(\boldsymbol{x}, t) = c_0 + c'(\boldsymbol{x}, t), \tag{3.9}$$

resulting in a small velocity disturbance $\boldsymbol{u}(\boldsymbol{x}) = \boldsymbol{u}'(\boldsymbol{x})$, and a small deformation of the particles through the disturbance rate of strain and the linearized mobility equation (3.1). Substituting these perturbations into the conservation equation for the particle concentration and neglecting nonlinear products of perturbations leads to the following linearized equation for the concentration fluctuations:

$$\frac{\partial c'}{\partial t} + M_0\boldsymbol{F}\cdot\nabla c' + c_0\nabla\cdot(\boldsymbol{u}' + \tau_s M_0\boldsymbol{E}'\boldsymbol{F}) - \nabla\cdot(\boldsymbol{D}\nabla c') = 0. \tag{3.10}$$

Assume a normal mode perturbation of a given wavevector $\boldsymbol{k}$:

$$c'(\boldsymbol{x}, t) = \tilde{c}(\boldsymbol{k})\exp \mathrm{i}(\boldsymbol{k}\cdot\boldsymbol{x} - \omega t). \tag{3.11}$$

The resulting disturbance velocity can be written: $\boldsymbol{u}'(\boldsymbol{x}, t) = \tilde{\boldsymbol{u}}(\boldsymbol{k})\exp \mathrm{i}(\boldsymbol{k}\cdot\boldsymbol{x} - \omega t)$ where the Fourier coefficient $\tilde{\boldsymbol{u}}(\boldsymbol{k})$ was calculated analytically by Hasimoto (1959):

$$\tilde{\boldsymbol{u}}(\boldsymbol{k}) = \frac{1}{\mu k^2}\left(\boldsymbol{I} - \frac{\boldsymbol{k}\boldsymbol{k}}{k^2}\right)\cdot\boldsymbol{F}\tilde{c}(\boldsymbol{k}). \tag{3.12}$$

Noting that $\tilde{\boldsymbol{E}}'(\boldsymbol{k}) = \mathrm{i}(\tilde{\boldsymbol{u}}'\boldsymbol{k} + \boldsymbol{k}\tilde{\boldsymbol{u}}')/2$, and that $\boldsymbol{k}\cdot\tilde{\boldsymbol{u}}' = 0$ from continuity, equation (3.10) simplifies to:

$$-\mathrm{i}\omega\tilde{c} + \mathrm{i}M_0\boldsymbol{F}\cdot\boldsymbol{k}\tilde{c} - \frac{\tau_s c_0 M_0}{2\mu}\boldsymbol{F}\cdot\left(\boldsymbol{I} - \frac{\boldsymbol{k}\boldsymbol{k}}{k^2}\right)\cdot\boldsymbol{F}\tilde{c} + \boldsymbol{k}\cdot(\boldsymbol{D}\boldsymbol{k})\tilde{c} = 0. \tag{3.13}$$

Denote by θ the angle between the wavevector $\boldsymbol{k}$ and the direction of gravity: $\boldsymbol{k}\cdot\hat{\boldsymbol{z}} = k\cos\theta$, and let $\boldsymbol{F} = F\hat{\boldsymbol{z}}$. After manipulation, we can solve for the wave frequency

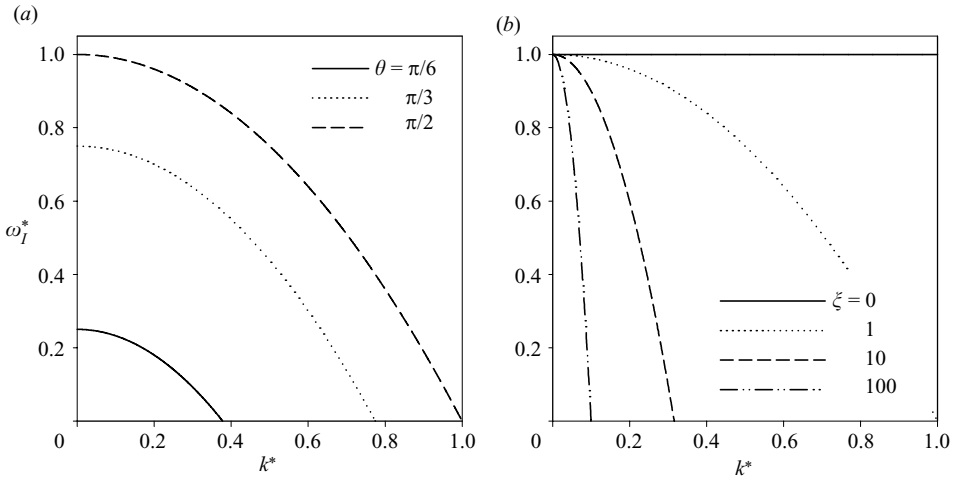

FIGURE 14. Growth rate as a function of the magnitude of the wavenumber: in dimensionless variables, $\omega_I^* = \sin^2\theta - \xi(k^*)^2(D_\parallel/D_\perp\cos^2\theta + \sin^2\theta)$, where ξ is a dimensionless diffusion constant (equation (3.17)). For both plots the ratio $D_\parallel/D_\perp$ of the diffusivities was chosen equal to 2. (*a*) shows the influence of the orientation angle θ of the wavevector with respect to the direction of gravity, at $\xi = 1$. (*b*) shows the influence of the diffusion coefficient ξ for a horizontal wave ($\theta = \pi/2$).

ω as a function of the magnitude k and orientation θ of the wavevector:

$$\omega = M_0 F k\cos\theta + \mathrm{i}\left[\frac{\tau_s c_0 M_0 F^2}{2\mu}\sin^2\theta - k^2(D_\parallel\cos^2\theta + D_\perp\sin^2\theta)\right]. \tag{3.14}$$

The frequency ω has a real part $\omega_R = M_0 F k\cos\theta = U_0 k\cos\theta$, which is non-zero for wavevectors with a vertical component, i.e. for density fluctuations in the vertical direction, and corresponds to travelling waves with a wave speed equal to the sedimentation velocity; such waves do not either grow or decay. The imaginary part of the frequency

$$\omega_I = \frac{\tau_s c_0 M_0 F^2}{2\mu}\sin^2\theta - k^2(D_\parallel\cos^2\theta + D_\perp\sin^2\theta) \tag{3.15}$$

is non-zero and positive at low wavenumbers for wavevectors with a horizontal component, provided that the constant τ_s is positive (which, as we argue in the following section, is the case in many situations). Low-wavenumber fluctuations in the horizontal direction will therefore amplify, and the growth rate is plotted *vs.* k for different values of the wave orientation θ and of the diffusivities $D_\perp$ and $D_\parallel$ in figure 14, in which the following dimensionless variables are used:

$$\omega_I^* = \omega_I \times \left[\frac{\tau_s c_0 M_0 F^2}{2\mu}\right]^{-1}, \quad k^* = k \times c_0^{-1/3}, \tag{3.16}$$

and where we introduce a dimensionless diffusion coefficient

$$\xi = \frac{2\mu D_\perp}{\tau_s c_0^{1/3} M_0 F^2}, \tag{3.17}$$

comparing the effects of diffusion and of the lateral convection due to deformations.

In the absence of hydrodynamic dispersion, equation (3.15) and figure 14(*b*) show that the growth rate is independent of the wavenumber, i.e. in the linear regime, all fluctuations grow at the same pace. This peculiar behaviour is a consequence of the linear dependence of the mobility correction on the disturbance rate of strain and of the slow decay of the disturbance velocity in sedimenting suspensions, both of which result in a migration flux scaling as $1/k$, and in a growth rate independent of k. The damping of the fluctuations shown in figure 14 is therefore purely a consequence of hydrodynamic dispersion: at a value of $\xi = 1$, diffusion dominates deformation-induced lateral migration over length scales of the order of the mean interparticle distance, hence the negative growth rates observed beyond $k^* = 1$. This mechanism is to be contrasted with the damping observed by Koch & Shaqfeh (1989) in the case of spheroids, where diffusion had been neglected. For spheroids, the decay at high wavenumbers is a consequence of the non-instantaneous relaxation of the particle orientation, whose characteristic time can be of the same order as the time for the spheroid to migrate over one wavelength at high enough wavenumbers. An equivalent way of looking at it is to recognize that the dispersion in orientation due to the initial random configuration leads to an effective dispersion of the centre-of-mass motion, qualitatively similar to the Taylor dispersion for Brownian systems (Brenner 1979). Introducing shape history effects (i.e. non-instantaneous shape relaxation) into our model would provide an additional mechanism for damping similar to the dispersion in orientation for rigid spheroids; however, as we will observe for droplets in § 3.2.1, including shape history would typically lead to $O(\epsilon^2)$ corrections in weak flows. It should also be noted that the continuum model developed here is not valid for fluctuations over length scales that are shorter than the interparticle distance, and the results described above are expected to break down at sufficiently high wavenumbers.

3.2. *Examples of deformable particles*

The previous model, for all its simplicity, is based on two strong assumptions whose applicability may not seem obvious: (i) that the particle shape relaxes instantaneously on the flow time scale; and (ii) that in weak flows the mobility of a slightly deformed particle can be written as a linear function of the local rate of strain with a positive constant of proportionality. In this section, we discuss in turn the small deformation of viscous drops, elastic microcapsules and flexible polymers, and show that all three of these satisfy both assumptions in the limit of weak flows.

3.2.1. *Viscous drops*

The small deformation of a viscous drop in a linear flow field was first studied by Taylor (1932, 1934) and later generalized by Cox (1969) and Frankel & Acrivos (1970). At zero Reynolds number, the deformation is a function of two dimensionless groups, namely the viscosity ratio $\lambda = \mu/\mu_0$ and the capillary number $Ca = \mu\dot{\gamma}a/\sigma$, where $\dot{\gamma}$ is the characteristic shear rate of the imposed flow field, a is the radius of the undeformed drop and σ is the surface tension. The capillary number compares the effect of the flow, which tends to stretch the drop along its extensional axis, to the restoring effect of surface tension, which tries to miminize the interfacial energy by maintaining a spherical shape. In the limit of weak flows ($Ca \ll 1$), the drop is found to deform into an ellipsoid whose surface is defined by:

$$r = a(1 + 3\,Ca\,\boldsymbol{n}\cdot\boldsymbol{A}\cdot\boldsymbol{n}) + O(Ca^2), \tag{3.18}$$

where $\boldsymbol{n}$ is a unit radial vector and $\boldsymbol{A}$ is a symmetric and traceless second-order tensor satisfying the following evolution equation:

$$Ca\left(\frac{\partial \boldsymbol{A}}{\partial t} - \boldsymbol{\Omega}\cdot\boldsymbol{A} + \boldsymbol{A}\cdot\boldsymbol{\Omega}\right) = a_0\boldsymbol{E} + a_1\boldsymbol{A} + O(Ca), \tag{3.19}$$

with $a_0 = 5/(6\lambda+9)$ and $a_1 = -40(\lambda+1)/\left[(2\lambda+3)(19\lambda+16)\right]$. $\boldsymbol{\Omega}$ and $\boldsymbol{E}$ are, respectively, the rate of rotation and rate of strain of the imposed flow; in equation (3.19), lengths have been non-dimensionalized by the drop radius a, and time by the inverse of the effective characteristic shear rate $\dot{\gamma}^{-1}$. At zeroth order in the capillary number, equation (3.19) leads to:

$$\boldsymbol{A} = -\frac{a_0}{a_1}\boldsymbol{E} = \frac{8(19\lambda+16)}{3(\lambda+1)}\boldsymbol{E} + O(Ca), \tag{3.20}$$

showing that the drop shape is only dependent upon the local rate of strain and not on the shape history (i.e. it relaxes instantaneously). Equation (3.18) then becomes:

$$r = a\left(1 + \frac{8(19\lambda+16)}{\lambda+1}\,Ca\,\boldsymbol{n}\cdot\boldsymbol{E}\cdot\boldsymbol{n}\right) + O(Ca^2). \tag{3.21}$$

The drop shape is therefore ellipsoidal, its principal axes are aligned with the principal axes of the local rate of strain, and it is stretched in the direction of flow extension. The sedimentation velocity of such a deformed drop placed in a gravity field was calculated by Haber & Hetsroni (1971) using expansions in spherical harmonics, and by Manga & Stone (1993) by application of the reciprocal theorem for Stokes flow. Both indeed find a correction to the sedimentation velocity which is linear in the rate of strain $\boldsymbol{E}$ for small deformations. The result from Haber & Hetsroni (1971) can be written as:

$$\boldsymbol{M}(\boldsymbol{E}) = M_0\left(\boldsymbol{I} + \frac{(19\lambda+16)(3\lambda^2+3\lambda+4)}{40(2+3\lambda)(1+\lambda)^2}\,Ca\,\boldsymbol{E} + O(Ca^2)\right), \tag{3.22}$$

where $M_0 = (1+\lambda)/2(2+3\lambda)\pi\mu a$ is the mobility of a spherical drop. Equation (3.22) is indeed similar to equation (3.1) with a positive constant τ_s.

3.2.2. *Elastic microcapsules*

Barthès-Biesel (1980) and Barthès-Biesel & Rallison (1981) developed a similar small-deformation theory for elastic microcapsules, which are particles consisting of an elastic membrane enclosing a drop of fluid. In this case, the dimensionless parameters are the viscosity ratio λ, and the ratio $\epsilon = \mu\dot{\gamma}a/Eh$ of the viscous stresses in the fluid and elastic tensions in the membrane, where E denotes the elastic modulus of the membrane material and h its thickness. In weak flows ($\epsilon \ll 1$), the shape is again found to be ellipsoidal, and to leading order in ϵ, the equation of the surface is obtained to be (Barthès-Biesel & Rallison 1981):

$$r = a\,(1 + f\epsilon\,\boldsymbol{n}\cdot\boldsymbol{E}\cdot\boldsymbol{n}) + O(\epsilon^2), \tag{3.23}$$

where f is a function of the material properties of the membrane; for an incompressible isotropic material in the small deformation regime: $f = 25/2$.

The mobility of an ellipsoidal capsule is simply the mobility of a solid ellipsoid, which is known exactly (for instance, Happel & Brenner 1965). In the case of small deformations, the mobility can be expanded in a Taylor series with respect to the spherical shape, and is found to be:

$$\boldsymbol{M}(\boldsymbol{E}) = M_0\left(\boldsymbol{I} + \tfrac{1}{5}f\epsilon\boldsymbol{E} + O(\epsilon^2)\right), \tag{3.24}$$

where $M_0 = 1/6\pi\mu a$ is the mobility of a solid sphere.

3.2.3. *Flexible polymers*

The applicability of the model to flexible polymers is less evident. In the absence of flow, a polymer molecule relaxes to a statistically isotropic coiled state as a result of internal Brownian motion. The application of a weak flow will lead to a small departure from this isotropic state, provided that the molecule can sample its configuration space sufficiently fast on the flow time scale, i.e. that its relaxation time is much faster than the inverse of the effective flow shear rate $\dot{\gamma}^{-1}$. The configuration of the molecule is then represented well by the average second moment of its end-to-end vector: $\boldsymbol{Q} = \langle \boldsymbol{R}\boldsymbol{R} \rangle$, and its mobility can be written in the general form:

$$\boldsymbol{M} = m\boldsymbol{I} + m'\boldsymbol{Q}. \tag{3.25}$$

In the simplest case of a linear spring law, the configuration tensor $\boldsymbol{Q}$ satisfies the following evolution equation (Bird *et al.* 1987):

$$Wi\left(\frac{\mathrm{d}}{\mathrm{d}t}\boldsymbol{Q} - \nabla\boldsymbol{u}\cdot\boldsymbol{Q} - \boldsymbol{Q}\cdot\nabla\boldsymbol{u}^T\right) + \boldsymbol{Q} - \frac{kT}{H}\boldsymbol{I} = 0. \tag{3.26}$$

Wi is the effective Weissenberg number defined as the ratio of the relaxation time of the molecule to the characteric flow time scale $\dot{\gamma}^{-1}$, kT is the thermal energy of the solvent, and H is the spring constant. For weak flows ($Wi \ll 1$), the configuration tensor can be solved for as a perturbation expansion in powers of the Weissenberg number: $\boldsymbol{Q} = \boldsymbol{Q}^{(0)} + Wi\,\boldsymbol{Q}^{(1)} + O(Wi^2)$, yielding:

$$\boldsymbol{Q} = \frac{kT}{H}\left(\boldsymbol{I} + Wi\,\left(\nabla\boldsymbol{u} + \nabla\boldsymbol{u}^T\right)\right) + O(Wi^2). \tag{3.27}$$

The mobility of the molecule equation (3.25) then becomes:

$$\boldsymbol{M}(\boldsymbol{E}) = \left(m + m'\frac{kT}{H}\right)\boldsymbol{I} + 2m'\frac{kT}{H}\,Wi\,\boldsymbol{E} + O(Wi^2) \tag{3.28}$$

and is again in the form of equation (3.1).

3.3. *Simulation method for deformable particles*

The simulation method described in § 2.1 for spheroids is easily adapted to the case of deformable particles, using the model of § 3.1.1. The motion of a particle α is described by the following dynamic equation:

$$\dot{\boldsymbol{x}}_\alpha = \boldsymbol{M}(\boldsymbol{x}_\alpha)\cdot\boldsymbol{F} + \boldsymbol{u}(\boldsymbol{x}_\alpha), \tag{3.29}$$

in which the linearized mobility of equation (3.1) is used:

$$\boldsymbol{M}(\boldsymbol{x}_\alpha) = M_0\left(\boldsymbol{I} + \tau_s\boldsymbol{E}(\boldsymbol{x}_\alpha)\right). \tag{3.30}$$

Hydrodynamic interactions are again captured through the disturbance velocity field $\boldsymbol{u}$ which is obtained as a solution of the Stokes equations (2.5) with the same body force field equation (2.8) as in the case of spheroids. The velocity $\boldsymbol{u}$ is used to infer the disturbance rate of strain $\boldsymbol{E}$ at the particle positions, which appears in the particle mobility equation (3.30). The Stokes equations are again solved spectrally on a grid, as explained in § 2.1.3. The particle positions are advanced using a fourth-order Runge-Kutta time-marching scheme. Unless noted otherwise, the results shown are for non-periodic systems with slip boundary conditions.

In the following discussion, the results are made dimensionless using the characteristic radius a of an undeformed particle, the sedimentation velocity $U_0 = M_0 F$

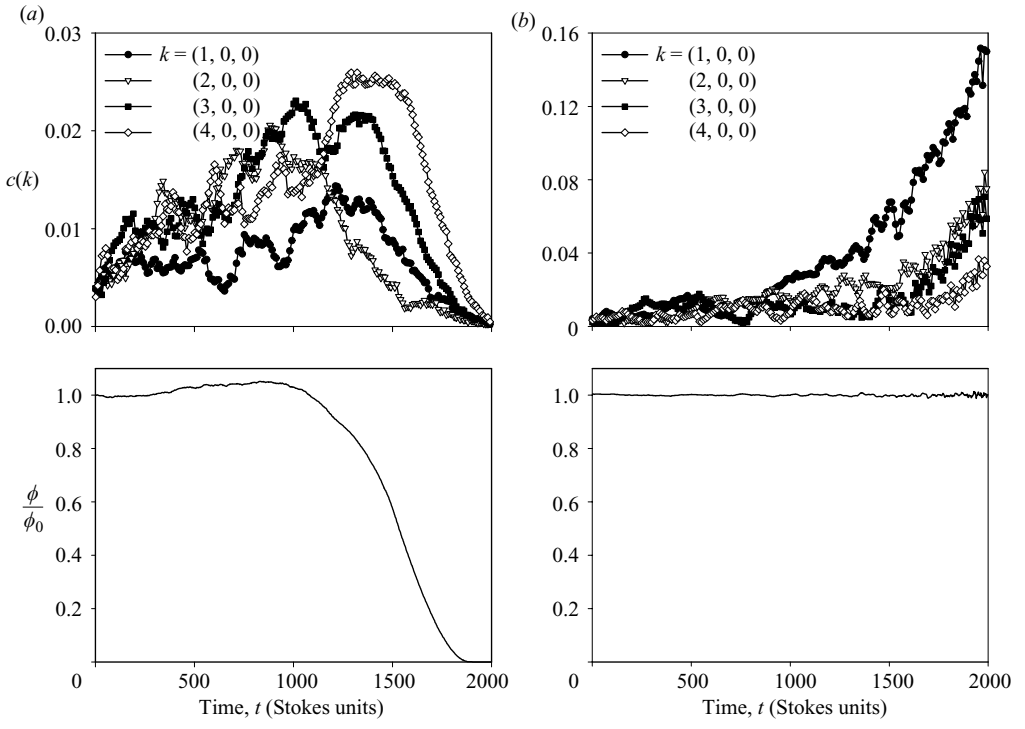

FIGURE 15. Time evolution of the Fourier coefficients of the concentration for a simulation of 158 239 deformable particles in a box of dimensions $L_x = 390$, $L_y = 390$ and $L_z = 2200$ (volume fraction $\phi = 0.2\%$), in both (a) non-periodic and (b) periodic boundary conditions. The results shown are for $\epsilon = 0.5$ and $r = 15$. The spectra were calculated over a subsection of the container: $250 < z < 650$, and were averaged over four runs. The lower plots show the evolution of the mean volume fraction in the section in which the spectra were obtained.

of an isolated particle, and the characteristic time a/U_0 for an isolated particle to sediment over its radius. A precise non-dimensionalization of the equations yields two dimensionless groups (in addition to the volume fraction ϕ): a deformation parameter $\epsilon = \tau_s U_0/a$, which characterizes the effect of the flow on the shape deformation (in the case of droplets ϵ is essentially the Bond number or capillary number based on the shear rate induced by the sedimentation of a drop, modified to include the function of the viscosity ratio in equation (3.22)), and a resistance parameter $r = \Delta\rho V_p g/\mu U_0 a$, which takes on the value of 6π for a solid particle and of $2\pi(2 + 3\lambda)/(1 + \lambda)$ for a viscous droplet. Most of the results presented below are for a deformation parameter of $\epsilon = 0.5$ (which as we verify in § 3.5 does indeed lead to small deformations at the volume fractions considered in this work), and a resistance parameter of $r = 15$, corresponding approximately to a drop with a viscosity ratio of 1. For the sake of comparison, a few results are also shown for spherical particles, obtained by setting the deformation parameter ϵ to zero.

3.4. *Concentration fluctuations and microstructure*

The same type of analysis as in the case of spheroids can be carried out for deformable particles. Figure 15 shows the evolution of a few Fourier coefficients of the concentration field in non-periodic and periodic systems. Initially, all Fourier modes are equally important. In the periodic case (figure 15b), no significant growth

is observed up to 1000 time units, after which all four modes start growing. As in the case of spheroids and as predicted by the linear stability analysis (equation (3.15) and figure 14), the longest mode $\boldsymbol{k}=(1,0,0)$, set by the width of the box, dominates; the growth is exponential and does not seem to saturate. As expected, the non-periodic case is quite different. The fluctuations are typically much weaker and the longest mode is not the strongest. Figure 15(*a*) shows that all modes initially grow at the same pace. The longest modes $\boldsymbol{k}=(1,0,0)$ and $\boldsymbol{k}=(2,0,0)$, however, stop growing, giving way progressively to the growth of the shorter modes $\boldsymbol{k}=(3,0,0)$ and $\boldsymbol{k}=(4,0,0)$ which dominate up to the arrival of the suspension front (lower plot) and the decay of the fluctuations.

As in the case of spheroids, figure 15 suggests that the presence of walls and the possibility of stratification provide a mechanism for the breakup of the longest modes into fluctuations at shorter wavelengths, which are then observed to dominate the spectrum. In spite of the strong similarity between the sedimentation of orientable and deformable particles, the two situations also present some differences. In the case of deformable particles, the growth is much more progressive and slow: the peak of the fluctuations occurs quite late during the sedimentation process. For spheroids, however, the growth of the fluctuations was rapid initially, after which it was found to saturate in non-periodic systems and to slow down in periodic systems (figure 2). This qualitative difference can be explained in the following way. In the case of spheroids, we saw in figure 10 that the fluctuations in the fluid result in a very quick alignment of the particles in the direction of gravity. Once most particles are aligned, migration becomes rather difficult, as the lateral velocity of an almost vertical spheroid is weak: further clustering is therefore limited. In the case of deformable particles, however, the stretching of the particles occurs along the axis of flow extension which is at 45° in shear flow, and migration is therefore quite easy, even though the deformations may be small. Moreover, as we will show in § 3.5, deformations become larger with time, allowing for a steady increase of the concentration fluctuations, whereas for spheroids the orientation distribution quickly reaches a steady state. This explains why the instability takes a longer time to develop, and similar observations will be made on the mean velocity and velocity fluctuations in § 3.6.

Figure 16 shows the pair distribution function and the structure factor in the lateral direction at $t=0$ and $t=1200$, for both deformable particles ($\epsilon=0.5$) and isotropic particles such as rigid spheres ($\epsilon=0$). At $t=0$, the pair distribution is uniform in both cases, and no clear peak is present in the structure factor. In the case of deformable particles, $g(x)$ progressively develops oscillations and a peak near $x=0$; while these are not as pronounced as in figure 4 for spheroids, the data of figure 16 are less noisy and the oscillations clearer. These oscillations result in a sharp peak in the structure factor at $t=1200$, which is located near $k=3$. A similar structure to that for spheroids is therefore present in the suspension, with denser regions or clusters alternating in the lateral direction with clear fluid. The evolution of the structure factor with time (not shown), also suggests that the formation of this structure is the consequence of the breakup of long-wavelength fluctuations. In the case of undeformed isotropic particles ($\epsilon=0$), no clear evolution of the pair distribution function or structure factor can be seen, and the fluctuations at $t=1200$ remain negligible. This confirms the central role of shape anisotropy in the concentration instability observed in suspensions of either spheroids or deformable particles.

Results on the stratification are also shown in figure 17 for both deformable and isotropic particles. The deformable case (figure 17*a*) is qualitatively similar to the case of spheroids shown in figure 3. In particular, a broad suspension front is observed to

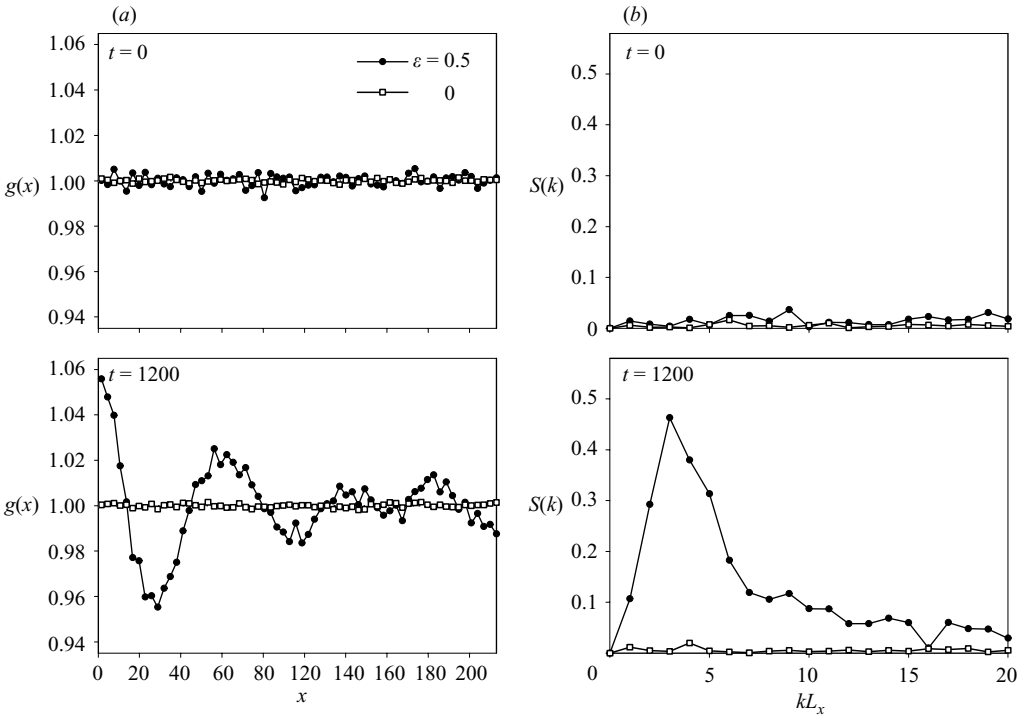

FIGURE 16. (*a*) Pair distribution function and (*b*) structure factor at $t=0$ and $t=1200$ for a simulation of 148 349 particles in a box of dimensions $L_x=390$, $L_y=145$ and $L_z=2200$ (volume fraction $\phi=0.5\%$). The plots show results for both deformable particles ($\epsilon=0.5$) and isotropic particles such as rigid spheres ($\epsilon=0$), at the same resistance parameter of $r=15$.

form between the bulk of the suspension and the clear fluid at the top; concentrations exceeding the bulk average are also observed near the bottom of the box as a result of clustering. As in the case of spheroids, this strong stratification is a consequence of the anisotropic mobility of the particles, which acts like a polydispersity, and of the segregation of the clusters near the bottom of the container. Note that neither of these effects is present in the case of isotropic particles (figure 17*b*), where the interface between the suspension and the clear fluid is sharp and does not show any significant broadening, and where the concentration in the suspension remains uniform in the vertical direction and equal to the mean bulk value.

3.5. *Particle deformation*

It is important to verify *a posteriori* that the deformation of the particles in the simulations remains small. As the particle shape or configuration is not explicitly calculated in the simulation method, but only its mobility, we define an effective aspect ratio A as the ratio of the largest to the smallest of the eigenvalues of the mobility tensor. This ratio, which is 1 for a spherical particle, but would approach 2 for a very slender particle, is indeed a measure of the anisotropy. Figure 18(*a*) shows the evolution of A at various volume fractions, for a deformation parameter ϵ of 0.5. All three curves present an initial increase of the effective aspect ratio as a result of the instability, followed by a decrease as the front approaches and as the fluctuations decay in the suspension. At low volume fractions ($\phi=0.1\%$), the particles remain very close to isotropic, with a mean aspect ratio of less than 1.01. Deformations become more

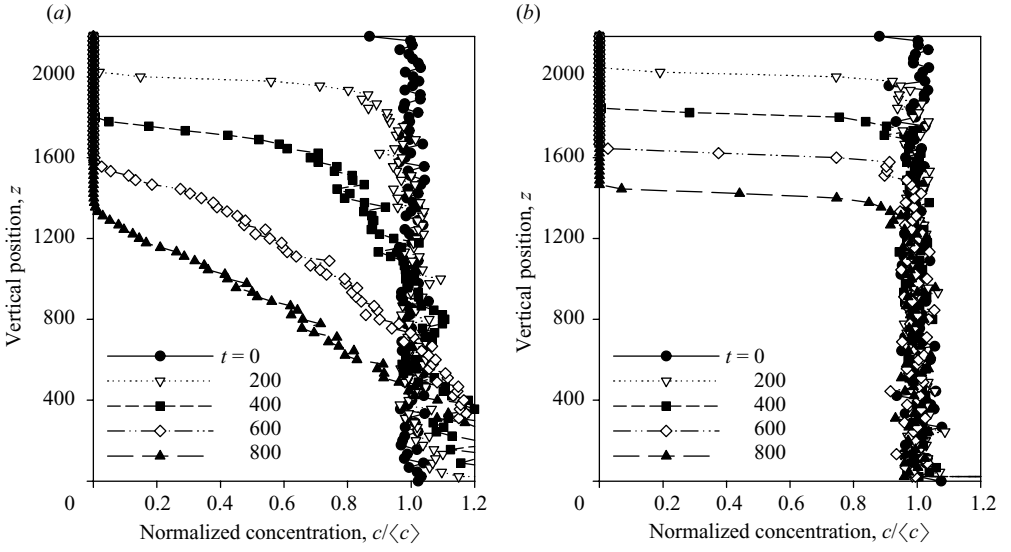

FIGURE 17. Cross-section averaged concentration profile in the vertical direction at various times during the sedimentation of suspensions of (*a*) deformable particles ($\epsilon = 0.5$), and (*b*) isotropic particles ($\epsilon = 0$). The results are for a resistance parameter of $r = 15$ and were obtained in suspensions of 148 349 particles in a box of dimensions $L_x = 390$, $L_y = 145$, $L_z = 2200$ (volume fraction $\phi = 0.5\%$). The concentration profile is normalized by its average value $\langle c \rangle$.

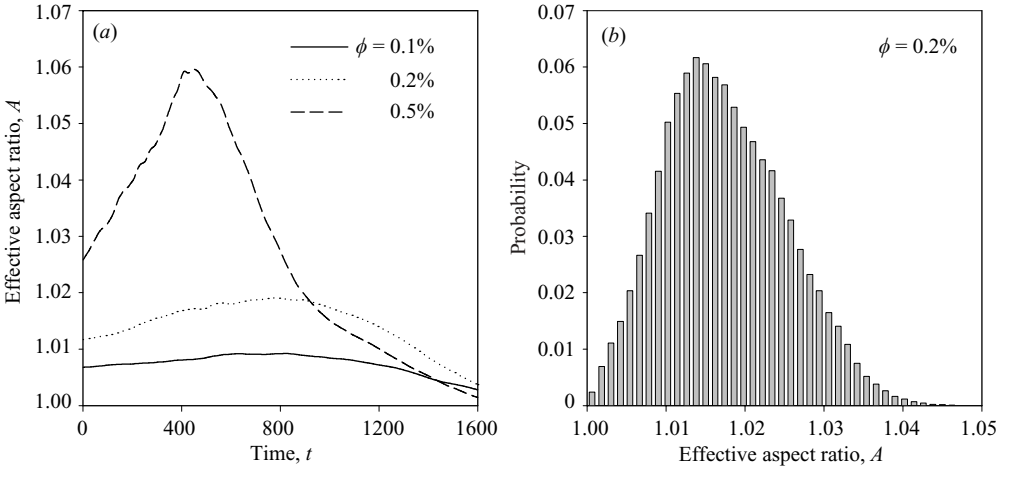

FIGURE 18. (*a*) Time evolution of the mean effective aspect ratio A at different volume fractions, and (*b*) distribution of the effective aspect ratio at a volume fraction of $\phi = 0.2\%$. The simulations are for $\epsilon = 0.5$ and $r = 15$ and were performed in a box of dimensions $L_x = 390$, $L_y = 145$, $L_z = 2200$. The results were obtained in a subsection of the box: $550 < z < 850$, and are averaged over ten runs.

significant at higher concentrations as a result of the stronger velocity fluctuations; nevertheless, the mean aspect ratio does not exceed 1.06 even at the highest volume fraction of 0.5%, therefore validating our small-deformation assumption. A typical distribution for the aspect ratio is shown in figure 18(*b*) at $\phi = 0.2\%$: while the mean value falls slightly below 1.02, aspect ratios in the suspension range from 1 up to

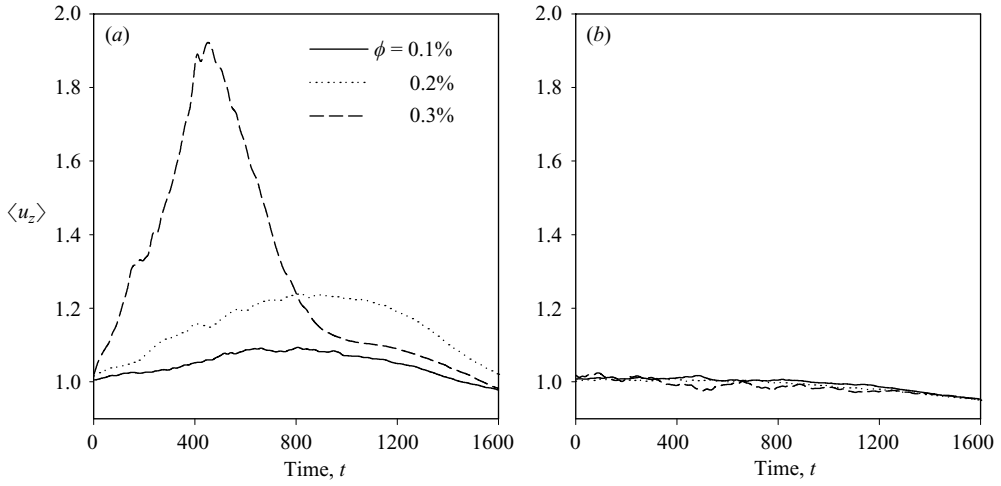

FIGURE 19. Mean sedimentation velocity $\langle u_z \rangle$ in suspensions of (a) deformable particles ($\epsilon = 0.5$), and (b) isotropic particles ($\epsilon = 0$) for a resistance parameter of $r = 15$ and at various volume fractions. The simulations were performed in a box of dimensions $L_x = 390$, $L_y = 145$, $L_z = 2200$. The results were obtained in a subsection of the box: $550 < z < 850$, and are averaged over ten runs.

nearly 1.05. This shape polydispersity is a natural consequence of the inhomogeneous flow field: the particles located in regions of strong shear typically undergo stronger deformations than those located near the local extrema of the disturbance velocity.

Note that larger deformations may have been expected given the value chosen for the deformation parameter ($\epsilon = 0.5$). This is a consequence of the length scale used in the definition of ϵ (the particle radius a), which can differ significantly from the characteristic length scale l_c over which the velocity fluctuations occur in the suspension. Typically, the disturbance velocity varies over distances that are much larger than a (up to the width L of the container during the initial instants), leading to velocity gradients scaling with U_0/l_c. A more appropriate deformation parameter would be $\epsilon = \tau_s U_0/l_c$; however, the fact that l_c is unknown *a priori* and evolves during the sedimentation process makes this definition awkward.

3.6. *Velocity statistics*

As in the case of spheroids, the particle deformations and the clustering have a strong impact on the sedimentation rate and the velocity fluctuations. This is illustrated in figures 19 and 20, where results for deformable ($\epsilon = 0.5$) and isotropic ($\epsilon = 0$) particles are compared at various volume fractions. The mean sedimentation speed in both cases is shown in figure 19. In the case of deformable particles, figure 19(a) shows a slow and steady increase of the mean sedimentation speed beyond the velocity of 1 of an isolated isotropic particle; this enhancement of the velocity is to be contrasted with the results of figure 19(b) in the absence of deformations, where the mean velocity is approximately constant and equal to 1 at all three volume fractions. Note that, in reality, a dependence on volume fraction will be observed in suspensions of spherical particles, as fluid backflow results in velocity hindrance (e.g. Batchelor 1972); this effect, however, cannot be captured at the point-force level used in our simulations. While the velocity increase in figure 19(a) is quite weak at low volume fractions (owing to the small deformations resulting in a weak instability), it becomes quite significant at $\phi = 0.5\%$ where the mean velocity reaches a peak value beyond 1.9.

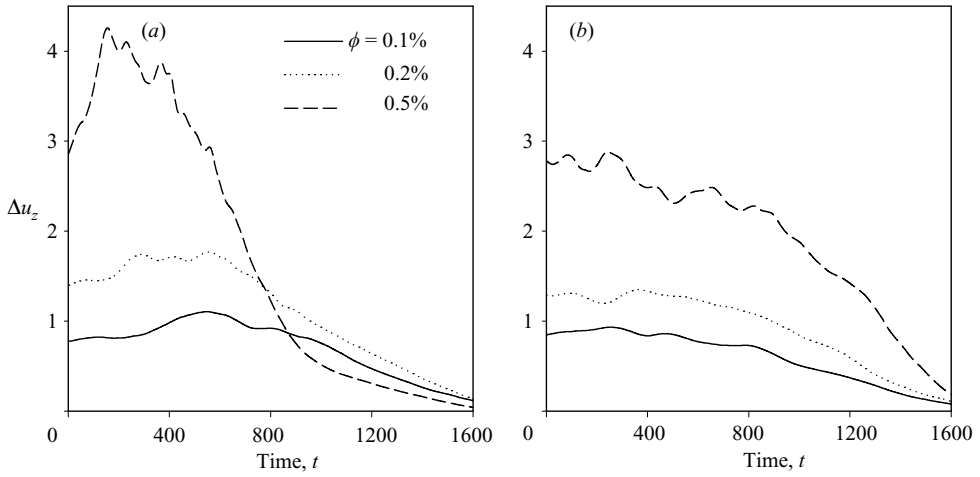

FIGURE 20. Velocity variance in the z-direction Δu_z in suspensions of (a) deformable particles ($\epsilon = 0.5$), and (b) isotropic particles ($\epsilon = 0$) for a resistance parameter of $r = 15$ and at various volume fractions. The simulations were performed in a box of dimensions $L_x = 390$, $L_y = 145$, $L_z = 2200$. The results were obtained in a subsection of the box: $550 < z < 850$, and are averaged over ten runs.

This very drastic increase is mainly a consequence of the clustering, as the particle mobility at $\phi = 0.5\%$ was shown in figure 18 to differ by less than 10% from isotropy. Again the velocities are observed to decay as the front becomes nearer and as the concentration fluctuations become weaker.

The very high value for the sedimentation speed at $\phi = 0.5\%$ may seem surprising when compared to the case of prolate spheroids where the peak velocity was also slightly slightly less than 2 at the same volume fraction (figure 8). This can be understood in the light of the comments made in § 3.4; in the case of spheroids, the strong and rapid alignment in the vertical direction somewhat hinders the lateral migration of the particles after a short initial time. For deformable particles, however, the steady increase in the effective aspect ratio and the orientation of the particles along the direction of flow extension result in a prolonged clustering and in the steady increase of the mean velocity.

The velocity fluctuations in the vertical direction are shown in figure 20. While figure 20(b) shows a decay of the fluctuations in the case of isotropic particles, confirming observations made in previous studies (e.g. Bergougnoux *et al.* 2003; Mucha *et al.* 2004), the instability in the deformable case causes an initial increase in the fluctuations, followed by a steady decrease towards zero; no steady state is reached. The initial increase, which is a result of the deformations and of the clustering, leads to very strong fluctuations at the highest volume fraction of $\phi = 0.5\%$, where they reach up to 4 times the sedimentation speed of an isotropic particle. The subsequent decay of the fluctuations also appears to be somewhat faster with deformable particles, a possible consequence of the strong stratification that is observed to develop in the suspension (Luke 2000).

3.7. *Hydrodynamic dispersion*

The decay of high-wavenumber fluctuations in the stability analysis of § 3.1.3 was attributed to hydrodynamic dispersion. As we previously mentioned, it is an established result that particles in sedimenting suspensions undergo a diffusive

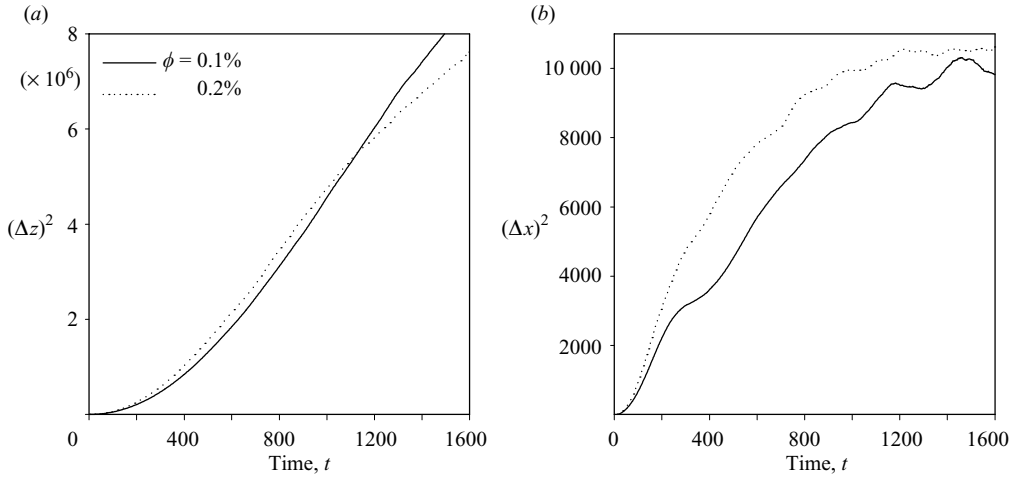

FIGURE 21. Mean squared displacement (a) in the z-direction and (b) in the x-direction at various volume fractions. The simulations are for $\epsilon = 0.5$ and $r = 15$ and were performed in a box of dimensions $L_x = 390$, $L_y = 145$, $L_z = 2200$; the results are averaged over three runs. For (a) the displacements were measured with respect to the mean motion of the entire suspension.

motion at long times relative to the mean settling motion and as a result of random fluctuations in the velocity field. In an attempt to understand the qualitative influence of the concentration fluctuations on hydrodynamic dispersion, mean-squared displacement curves were calculated and are shown in figure 21. All curves have a zero derivative at $t = 0$ and show a convective behaviour at short times: $(\Delta x)^2 \sim t^2$, $(\Delta z)^2 \sim t^2$. The slopes progressively stop increasing and a transition to a different regime occurs. The motion in the vertical direction becomes clearly diffusive, as suggested by the nearly constant slope in figure 21(a): $(\Delta z)^2 \sim D_{\|} t$. While confirming the diffusive nature of the particle motions, figure 21(a) should not be expected to produce quantitative results for the diffusivity, since close particle interactions and short-scale variations of the velocity field, both of which play an important part in the diffusion process, have been completely neglected in the simulations.

Diffusion is much less clear in the lateral direction (figure 21b), in which the mean-squared displacement slowly saturates to a constant value. This saturation could have several origins: in particular, lateral displacements are limited owing to the finite extent of the simulation box. It is also possible that the arrangement of the particles into dense clusters confines the lateral diffusion to the extent of one streamer; this seems to be supported by the steady-state value of $\Delta x \simeq 100$ in figure 21(b), which is of the order of a quarter of a box width. A more precise investigation is required to confirm this hypothesis.

4. Conclusions

We used a combination of large-scale numerical simulations and theory to study the sedimentation of orientable particles such as spheroids, and deformable particles such as viscous droplets. Our analysis focused on the concentration fluctuations and the microstructure in very dilute suspensions of realistic sizes. The concentration instability in suspensions of spheroids was captured in our simulations, and we observed that the no-flux boundary condition imposed at the bottom of the container has a strong impact on the structure of the suspension and can lead to a wavenumber

selection for the concentration fluctuations. This result differs qualitatively from previous computational studies of periodic systems, in which the longest wavelength set by the width of the container always dominates. Our simulations suggest that horizontal container boundaries provide a mechanism for the decay or breakup of these long-wavelength fluctuations, down to the selected wavelength of the instability. Although the precise mechanism for this breakup is not entirely clear, it appears to be qualitatively analogous to the suppression of low-wavenumber horizontal density fluctuations in suspensions of rigid spheres (Lei *et al.* 2001; Nguyen & Ladd 2004, 2005), which may be a consequence of homogenization by recirculation currents (Hinch 1987). Results for the velocity and orientation statistics showed good agreement with previous published experiments; in particular, these statistics were found not to depend upon the size and aspect ratio of the sedimenting system, unlike in previous simulations with periodic boundary conditions.

A simple model was developed for sedimenting suspensions of deformable particles, which is equally applicable to viscous droplets, elastic microcapsules or flexible polymers. Under the assumptions that the flow-induced deformations are small and that the relaxation of the particle shape or configuration occurs instantaneously on the flow time scale, we were able to perform a linear stability analysis and to prove that such suspensions are unconditionally unstable to horizontal density fluctuations. The analysis, based on a dilute assumption in an unbounded domain, shows that in the absence of centre-of-mass dispersion, all wavenumbers are equally unstable. Hydrodynamic dispersion is predicted to damp high-wavenumber fluctuations, resulting in a maximum growth rate at zero wavenumber.

Point-particle simulations were also performed for deformable particles, confirming the mechanism for the instability. Density fluctuations in the particle distribution are observed to grow in time as a result of the deformation of the particles, which leads to a lateral migration; the growth of the fluctuations is typically slower, but more steady than in suspensions of spheroids. The simulation results manifest a qualitatively similar mechanism for the wavenumber selection: while the longest wavelength grows unbounded in periodic systems, this mode is observed to break up in non-periodic geometries, resulting in the formation of distinct clusters separated by clarified regions in the lateral direction. The instability for deformable particles also causes an increase in the mean sedimentation velocity, and our simulations suggest that quite small departures from isotropy can have very strong effects. To our knowledge, no experimental data are available for comparison, but we hope that the present observations will spur additional interest in this problem.

Several effects were neglected in our simulation method, which is based on a dilute assumption and does not account for close particle interactions. In suspensions of spheroids, lubrication forces and excluded volume can lead to entanglements whose effects are not described by far-field hydrodynamics. These interactions, which may play a role inside the dense clusters and certainly become important in more concentrated suspensions, may affect the typical size of the clusters, as well as statistical properties such as the orientation distributions and the mean velocity. In particular, experiments on fibre suspensions suggest that in the semi-dilute and concentrated regimes entanglements lead to the formation of large networks of fibres and to velocity hindrance (Turney *et al.* 1995; Herzhaft & Guazzelli 1999); additional work is required to model these regimes. In the case of deformable particles, the effects of short-range interactions will depend on the precise nature of the particles. Zinchenko & Davis (2000, 2003) addressed the case of very concentrated emulsions ($\phi \sim 0.5$); the non-local nature of the flow and the lubrication interactions

between neighbouring drops result in complex drop deformations that cannot be adequately captured by the small-deformation model used in our work. In emulsions, the concentration instability may also enhance drop coalescence and therefore increase polydispersity; coalescence during sedimentation, which was previously studied using population dynamics (e.g. Manga & Stone 1995; Wang & Davis 1995), could be incorporated into our simulations using similar phenomenological collision models.

The authors are grateful to Bloen Metzger and Élisabeth Guazzelli for extensive discussions on their experiments and valuable comments on this work. D. S. acknowledges the hospitality of Groupement Écoulements de Particules at Institut Universitaire des Systèmes Thermiques Industriels (IUSTI), Marseille, France, where part of this work was initiated. We also thank John M. Rallison for bringing the work of Hetsroni & Haber (1970) and Haber & Hetsroni (1971) to our attention.

Appendix. Numerical accuracy of the Stokes flow solution

The solution of the Stokes equations described in § 2.1.3 is based on a few approximations, the effects of which are investigated in this Appendix. First, we study the effects of the tangential flow boundary condition at the container walls in § A.1, where we provide a comparison to a more accurate solution satisfying the no-slip boundary condition on two of the vertical walls. The effects of the grid resolution (number of Fourier modes) are then discussed in § A.2.

A.1. *Effect of the tangential flow boundary condition*

Our simulations have shown the importance of the no-flux boundary condition for the fluid at the bottom of the container, which is responsible for large-scale recirculation and appears to play a central role in the wavenumber selection of the concentration instability. While the no-flux condition is crucial at the bottom wall, previous investigations have suggested that the no-slip boundary condition on the container sidewalls may play a part in the damping of the velocity fluctuations (e.g. Brenner 1999; Mucha *et al.* 2004). The Green's function for Stokes flow is indeed strongly affected in confined geometries, where hydrodynamic interactions decay faster and are effectively screened over distances of the order of the shortest wall separation.

While the Green's function for Stokes flow between two parallel walls is known (Liron & Mochon 1976; Bhattacharya & Bławzdziewicz 2002; Staben, Zinchenko & Davis 2003; Jones 2004), no analytical form exists in the case of finite containers such as those considered in this work. For the purpose of comparison with the slip solution used in our work, we implemented the Green's function proposed by Mucha *et al.* (2004), which satisfies the no-slip boundary condition on two of the sidewalls (typically the two closest ones) and a tangential flow boundary condition on the remaining walls. This Green's function uses expansions in Fourier series in the two directions parallel to the no-slip walls, which are typically truncated at a finite number of modes; yet the absence of periodicity in the third direction precludes the use of fast Fourier transforms as for the slip solution, resulting in a higher computational cost for the evaluation of hydrodynamic interactions. See the Appendix of Mucha *et al.* (2004) for a detailed discussion of the no-slip solution.

Results of the comparison are summarized in table 2, where we show the effects of the boundary condition on the mean velocity and velocity fluctuations. These two quantities were calculated with either of the two Green's functions for a series

		Slip		No-slip	
Time	Window	$\langle u_z \rangle$	Δu_z	$\langle u_z \rangle$	Δu_z
$t = 0$	$0 < z < 180$	0.79	1.20	0.78	0.59
	$45 < z < 67.5$	0.83	1.17	0.79	0.61
$t = 20$	$0 < z < 180$	1.38	2.43	1.18	1.12
	$45 < z < 67.5$	1.52	3.09	1.21	1.19
$t = 40$	$0 < z < 180$	1.18	1.35	1.03	0.87
	$45 < z < 67.5$	1.21	1.60	1.11	0.98
$t = 60$	$0 < z < 180$	1.15	1.20	1.05	0.89
	$45 < z < 67.5$	1.13	1.47	1.05	0.85
$t = 80$	$0 < z < 180$	1.06	0.85	1.06	0.80
	$45 < z < 67.5$	1.10	0.91	1.07	0.80

TABLE 2. Influence of the flow boundary condition on the container sidewalls. Average sedimentation velocities $\langle u_z \rangle$ and velocity fluctuations in the vertical direction Δu_z were evaluated for a set of particle configurations corresponding to various stages during sedimentation ($t = 0$ to 80), using the tangential flow boundary condition described in § 2.1.3 ('slip'), and the Green's function of Mucha *et al.* (2004), which satisfies the no-slip boundary condition on two of the sidewalls ('no-slip'). The particle configurations used were obtained from a full simulation using the tangential flow boundary condition, in a suspension of 29 702 spheroids of aspect ratio $A = 15$ in a box of dimensions $L_x = 32$, $L_y = 12$, $L_z = 180$ (volume fraction $\phi = 0.1\%$). The statistics were calculated in two different windows: $0 < z < 180$ (entire container), and $45 < z < 67.5$ (same window as in figure 8).

		Number of Fourier modes					
		$16 \times 16 \times 64$		$32 \times 16 \times 128$		$64 \times 32 \times 256$	
Time	Window	$\langle u_z \rangle$	Δu_z	$\langle u_z \rangle$	Δu_z	$\langle u_z \rangle$	Δu_z
$t = 0$	$0 < z < 180$	0.81	1.82	.79	1.20	0.77	0.99
	$45 < z < 67.5$	0.84	1.85	.83	1.17	0.81	0.92
$t = 20$	$0 < z < 180$	1.36	2.98	.38	2.43	1.38	2.22
	$45 < z < 67.5$	1.54	3.75	.52	3.09	1.52	2.89
$t = 40$	$0 < z < 180$	1.09	1.93	.18	1.35	1.21	1.19
	$45 < z < 67.5$	1.17	2.31	.21	1.60	1.31	1.51
$t = 60$	$0 < z < 180$	1.06	1.60	1.15	1.20	1.22	1.32
	$45 < z < 67.5$	1.16	1.83	1.13	1.47	1.18	1.45
$t = 80$	$0 < z < 180$	0.96	1.13	1.06	0.85	1.18	0.98
	$45 < z < 67.5$	1.03	1.21	1.10	0.91	1.20	1.03

TABLE 3. Influence of the grid resolution on the accuracy of the Stokes flow solution. Average sedimentation velocities $\langle u_z \rangle$ and velocity fluctuations in the vertical direction Δu_z were evaluated for a set of particle configurations corresponding to various stages during sedimentation ($t = 0$ to 80), for various grid resolutions (i.e. numbers of Fourier modes). The same particle configurations were used as in table 2, and the statistics were calculated in two different windows: $0 < z < 180$ (entire container), and $45 < z < 67.5$ (same window as in figure 8).

of particle configurations corresponding to various stages of the sedimentation in a suspension of spheroids. While the mean velocities are quite similar in both cases (albeit somewhat higher with slip boundaries), table 2 shows that velocity fluctuations are systematically overestimated when slip is allowed, by up to a factor of 2 at the

peak of the fluctuations. This result, which supports the previous conclusions of Brenner (1999) and Mucha *et al.* (2004), also explains some of the differences noted in § 2.5 between our simulation results and the experimental data of Herzhaft & Guazzelli (1999).

A.2. *Effect of the grid resolution*

The effects of the grid resolution (i.e. number of Fourier modes) on the sedimentation statistics were also investigated. The results of this study are summarized in table 3, which reports velocity statistics obtained using three different grid resolutions. Note that in the method described in §§ 2.1.2 and 2.1.3, an increase in the number of Fourier modes also results in the reduction of the extent of the force assignment function, so that in the limit of an infinite number of modes the exact solution for a point force (Dirac delta function) should be recovered. As shown in table 3, the effects of the grid resolution on the mean sedimentation velocity are negligible. The velocity fluctuations, however, are affected more strongly, and are observed to decrease as the number of modes increases; significant errors can be expected using very coarse grids. In the simulations described in this paper, we typically used of the order of 32 modes in the horizontal directions and 128 modes in the vertical direction.

REFERENCES

Barthès-Biesel, D. 1980 Motion of a spherical microcapsule freely suspended in a linear shear flow. *J. Fluid Mech.* **100**, 831–853.

Barthès-Biesel, D. & Rallison, J. M. 1981 The time-dependent deformation of a capsule freely suspended in a linear shear flow. *J. Fluid Mech.* **113**, 251–267.

Batchelor, G. K. 1972 Sedimentation of a dilute dispersion of spheres. *J. Fluid Mech.* **52**, 245–268.

Bergougnoux, L., Ghicini, S., Guazzelli, E. & Hinch, J. 2003 Spreading fronts and fluctuations in sedimentation. *Phys. Fluids* **15**, 1875–1887.

Bhattacharya, S. & Bławzdziewicz, J. 2002 Image system for Stokes-flow singularity between two parallel planar walls. *J. Math. Phys.* **43**, 5720–5731.

Bird, H. B., Curtiss, C. F., Armstrong, R. C. & Hassager, O. 1987 *Dynamic of Polymeric Liquids.* Wiley Interscience.

Brenner, H. 1979 Taylor dispersion in systems of sedimenting nonspherical Brownian particles. I. Homogeneous, centrosymmetric, axisymmetric particles. *J. Colloid Interface Sci.* **71**, 189–208.

Brenner, M. P. 1999 Screening mechanisms in sedimentation. *Phys. Fluids* **11**, 754–772.

Butler, J. E. & Shaqfeh, E. S. G. 2002 Dynamic simulations of the inhomogeneous sedimentation of rigid fibres. *J. Fluid Mech.* **468**, 205–237.

Caflisch, R. E. & Luke, J. H. C. 1985 Variance in the sedimentation speed of a suspension. *Phys. Fluids* **28**, 759–760.

Cox, R. G. 1969 The deformation of a drop in a general time-dependent fluid flow. *J. Fluid Mech.* **37**, 601–623.

Deserno, M. & Holm, C. 1997 How to mesh up Ewald sums. I. A theoretical and numerical comparison of various particle mesh routines. *J. Chem. Phys.* **109**, 7678–7693.

Frankel, N. A. & Acrivos, A. 1970 The constitutive equation for a dilute emulsion. *J. Fluid Mech.* **44**, 65–70.

Guazzelli, E. 2001 Evolution of particle-velocity correlations in sedimentation. *Phys. Fluids* **13**, 1537–1540.

Haber, S. & Hetsroni, G. 1971 The dynamics of a deformable drop suspended in an unbounded Stokes flow. *J. Fluid Mech.* **49**, 257–277.

Ham, J. M. & Homsy, G. M. 1988 Hindered settling and hydrodynamic dispersion in quiescent sedimenting suspensions. *Intl J. Multiphase Flow* **14**, 533–546.

Happel, J. & Brenner, H. 1965 *Low Reynolds Number Hydrodynamics,* pp. 220–227. Prentice Hall.

Hasimoto, H. 1959 On the periodic fundamental solutions of the Stokes equations and their application to viscous flow past a cubic array of spheres. *J. Fluid Mech.* **5**, 317–328.

Herzhaft, B. & Guazzelli, E. 1999 Experimental study of the sedimentation of dilute and semi-dilute suspensions of fibres. *J. Fluid Mech.* **384**, 133–158.

Herzhaft, B., Guazzelli, E., Mackaplow, M. B. & Shaqfeh, E. S. G. 1996 Experimental investigation of the sedimentation of a dilute fiber suspension. *Phys. Rev. Lett.* **77**, 290–293.

Hetsroni, G. & Haber, S. 1970 The flow in and around a droplet or bubble submerged in an unbound arbitrary velocity field. *Rheol. Acta* **9**, 488–496.

Hinch, E. J. 1987 Sedimentation of small particles. In *Disorder and Mixing* (ed. E. Guyon, J.-P. Nadal & Y. Pomeau), chap. 9, pp. 153–161. Kluwer.

Hockney, R. W. & Eastwood, J. W. 1981 *Computer Simulation Using Particles*. McGraw-Hill.

Jeffery, G. B. 1922 The motion of ellipsoidal particles immersed in a viscous fluid. *Proc. R. Soc. Lond.* A **102**, 161–179.

Jones, R. B. 2004 Spherical particle in Poiseuille flow between planar walls. *J. Chem. Phys.* **121**, 483–500.

Koch, D. L. 1994 Hydrodynamic diffusion in a suspension of sedimenting point particles with periodic boundary conditions. *Phys. Fluids* **6**, 2894–2900.

Koch, D. L. & Shaqfeh, E. S. G. 1989 The instability of a dispersion of sedimenting spheroids. *J. Fluid Mech.* **209**, 521–542.

Koch, D. L. & Shaqfeh, E. S. G. 1991 Screening in sedimenting suspensions. *J. Fluid Mech.* **224**, 275–303.

Kumar, P. & Ramarao, B. V. 1991 Enhancement of the sedimentation rates of fibrous suspensions. *Chem. Engng Commun.* **108**, 381–401.

Kuusela, E., Höfler, K. & Schwarzer, S. 2001 Computation of particle settling speed and orientation distribution in suspensions of prolate spheroids. *J. Engng Maths* **41**, 221–235.

Kuusela, E., Lahtinen, J. M. & Ala-Nissila, T. 2003 Collective effects in settling of spheroids under steady-state sedimentation. *Phys. Rev. Lett.* **90**, 094502.

Ladd, A. J. C. 1992 Dynamical simulations of sedimenting spheres. *Phys. Fluids* A **5**, 299–310.

Ladd, A. J. C. 1996 Hydrodynamic screening in sedimenting suspensions of non-Brownian spheres. *Phys. Rev. Lett.* **76**, 1392–1395.

Ladd, A. J. C. 2002 Effects of container walls on the velocity fluctuations of sedimenting spheres. *Phys. Rev. Lett.* **88**, 048301.

Lei, X., Ackerson, B. L. & Tong, P. 2001 Settling statistics of hard sphere particles. *Phys. Rev. Lett.* **86**, 3300–3303.

Liron, N. & Mochon, S. 1976 Stokes flow for a Stokeslet between two parallel flat plates. *J. Engng Maths* **10**, 287–303.

Lomholt, S. & Maxey, M. R. 2003 Force-coupling method for particulate two-phase flow: Stokes flow. *J. Comput Phys.* **184**, 381–405.

Luke, J. H. C. 2000 Decay of velocity fluctuations in a stably stratified suspension. *Phys. Fluids* **12**, 1619–1621.

Mackaplow, M. B. & Shaqfeh, E. S. G. 1998 A numerical study of the sedimentation of fibre suspensions. *J. Fluid Mech.* **376**, 149–182.

Manga, M. & Stone, H. A. 1993 Buoyancy-driven interactions between two deformable viscous drops. *J. Fluid Mech.* **256**, 647–683.

Manga, M. & Stone, H. A. 1995 Collective hydrodynamics of deformable drops and bubbles in dilute low Reynolds number suspensions. *J. Fluid Mech.* **300**, 231–263.

Maxey, M. R. & Patel, B. K. 2001 Localized force representations for particles sedimenting in Stokes flow. *Intl J. Multiphase Flow* **27**, 1603–1626.

Mor, R., Gottlieb, M., Mondy, L. A. & Graham, A. L. 2003 Effect of surfaces on the static distribution of orientations in suspensions of rod-like particles. *J. Rheol.* **47**, 19–36.

Mucha, P. J. & Brenner, M. P. 2003 Diffusivities and front propagation in sedimentation. *Phys. Fluids* **15**, 1305–1313.

Mucha, P. J., Tee, S.-Y., Weitz, D. A., Shraiman, B. I. & Brenner, M. P. 2004 A model for velocity fluctuations in sedimentation. *J. Fluid Mech.* **501**, 71–104.

Nguyen, N.-Q. & Ladd, A. J. C. 2004 Microstructure in a settling suspension of hard spheres. *Phys. Rev.* E **69**, 050401.

Nguyen, N.-Q. & Ladd, A. J. C. 2005 Sedimentation of hard-sphere suspensions at low Reynolds number. *J. Fluid Mech.* **525**, 73–104.

Nicolai, H. & Guazzelli, E. 1995 Effect of the vessel size on the hydrodynamic diffusion of sedimenting spheres. *Phys. Fluids* **7**, 3–5.

Nicolai, H., Herzhaft, B., Hinch, E. J., Oger, L. & Guazzelli, E. 1995 Particle velocity fluctuations and hydrodynamic self-diffusion of sedimenting non-Brownian spheres. *Phys. Fluids* **7**, 12–23.

Ramaswamy, S. 2001 Issues in the statistical mechanics of steady sedimentation. *Adv. Phys.* **50**, 297–341.

Reinhart, W. H., Singh, A. & Werner, S. 1989 Red blood cell aggregation and sedimentation: the role of cell shape. *Brit. J. Haematol.* **73**, 551–556.

Saintillan, D., Darve, E. & Shaqfeh, E. S. G. 2005 A smooth particle-mesh Ewald algorithm for Stokes suspension simulations: the sedimentation of fibers. *Phys. Fluids* **17**, 033301.

Schoenberg, I. L. 1973 *Cardinal Spline Interpolation*. SIAM, Philadelphia.

Segrè, P. N., Herbolzheimer, E. & Chaikin, P. M. 1997 Long-range correlations in sedimentation. *Phys. Rev. Lett.* **79**, 2574–2577.

Sierou, A. & Brady, J. F. 2001 Accelerated Stokesian dynamics simulations. *J. Fluid Mech.* **448**, 115–146.

Staben, M. E., Zinchenko, A. Z. & Davis, R. H. 2003 Motion of a particle between two parallel plane walls in low-Reynolds-number Poiseuille flow. *Phys. Fluids* **15**, 1711–1733.

Taylor, G. I. 1932 The viscosity of a fluid containing small drops of another fluid. *Proc. R. Soc. Lond.* A **138**, 41–48.

Taylor, G. I. 1934 The deformation of emulsions in definable fields of flow. *Proc. R. Soc. Lond.* A **146**, 501–523.

Tee, S.-Y., Mucha, P. J., Cipelletti, L., Manley, S., Brenner, M. P., Segrè, P. N. & Weitz, D. A. 2002 Long-range correlations in sedimentation. *Phys. Rev. Lett.* **89**, 054501.

Turney, M. A., Cheung, M. K., Powell, R. L. & McCarthy, M. J. 1995 Hindered settling of rod-like particles measured with magnetic resonance imaging. *AIChE J.* **41**, 251–257.

Wang, H. & Davis, R. H. 1995 Simultaneous sedimentation and coalescence of a dilute dispersion of small drops. *J. Fluid Mech.* **295**, 247–261.

Zinchenko, A. Z. & Davis, R. H. 2000 An efficient algorithm for hydrodynamical interaction of many deformable drops. *J. Comput Phys.* **157**, 539–587.

Zinchenko, A. Z. & Davis, R. H. 2003 Large-scale simulations of concentrated emulsion flows. *Phil. Trans. R. Soc. Lond.* A **361**, 813–845.